



A physical neural mass model framework for the analysis of oscillatory generators from laminar electrophysiological recordings

Roser Sanchez-Todo^{a,f}, André M. Bastos^b, Edmundo Lopez-Sola^a, Borja Mercadal^a, Emiliano Santarnecchi^c, Earl K. Miller^{d,e}, Gustavo Deco^{f,g,h,i}, Giulio Ruffini^{a,j,k,*}

^a Department of Brain Modeling, Neuroelectronics SL, Av. Tibidabo 47b, 08035 Barcelona, Spain

^b Department of Psychology and Vanderbilt Brain Institute, Vanderbilt University, Nashville, TN, United States

^c Precision Neuroscience & Neuromodulation Program, Gordon Center for Medical Imaging, Department of Radiology, Massachusetts General Hospital, Harvard Medical School, Boston, MA, USA

^d The Picower Institute for Learning and Memory, Massachusetts Institute of Technology, Cambridge, MA 02139, USA

^e Department of Brain and Cognitive Sciences, Massachusetts Institute of Technology, Cambridge, MA 02139, USA

^f Center of Brain and Cognition, Computational Neuroscience Group, Department of Information and Communication Technologies, Universitat Pompeu Fabra, Barcelona, Spain

^g Institut d'Investigacions de la Recerca i Estudis Avançats (ICREA), Passeig Lluís Companys 23, Barcelona, 08010, Spain

^h Department of Neuropsychology, Max Planck Institute for Human Cognitive and Brain Sciences, 04103 Leipzig, Germany

ⁱ School of Psychological Sciences, Monash University, Melbourne, Clayton, VIC 3800, Australia

^j Starlab Barcelona, Av. Tibidabo 47b, 08035 Barcelona, Spain

^k Haskins Laboratories, 300 George Street, New Haven, CT, 06511, USA

ARTICLE INFO

Keywords:

Laminar NMM
Local field potentials
LFP
Bipolar LFP
CSD
Relative power

ABSTRACT

Cortical function emerges from the interactions of multi-scale networks that may be studied at a high level using neural mass models (NMM) that represent the mean activity of large numbers of neurons. Here, we provide first a new framework called laminar NMM, or LaNMM for short, where we combine conduction physics with NMMs to simulate electrophysiological measurements. Then, we employ this framework to infer the location of oscillatory generators from laminar-resolved data collected from the prefrontal cortex in the macaque monkey. We define a minimal model capable of generating coupled slow and fast oscillations, and we optimize LaNMM-specific parameters to fit multi-contact recordings. We rank the candidate models using an optimization function that evaluates the match between the functional connectivity (FC) of the model and data, where FC is defined by the covariance between bipolar voltage measurements at different cortical depths. The family of best solutions reproduces the FC of the observed electrophysiology by selecting locations of pyramidal cells and their synapses that result in the generation of fast activity at superficial layers and slow activity across most depths, in line with recent literature proposals. In closing, we discuss how this hybrid modeling framework can be more generally used to infer cortical circuitry.

1. Introduction

Jansen and Rit's neural mass model (NMM¹) (Jansen and Rit, 1995) is an effective *lumped* mesoscale model of neuronal populations based on the work of Lopes Da Silva and van Rotterdam in the 1970s (van Rotterdam et al., 1982; Lopes da Silva et al., 1976; 1974). It describes cortical

column dynamics by capturing relevant physiological features at the mesoscale, but in its original form, it has some limitations. For example, it can easily represent oscillations only in one specific frequency band for each parameter configuration (David and Friston, 2003) (although it can represent multiband activity, its repertoire is constrained by the six-dimensional character of the equations), limiting its usefulness in modeling disorders with multifrequency alterations such as Alzheimer's (Palop and Mucke, 2016). This can be remedied by adding more neuronal populations to the original model (Sotero, 2016), as we do here. Furthermore, NMMs cannot *per se* generate measurements such as local field potentials (LFP) or derived quantities such as current source density (CSD) since these models are not mathematically embedded in a physical medium. They do, however, provide a handle on synaptic current sources and membrane potentials, where physics modeling can begin. While membrane potential may be sufficient for comparison with

* Corresponding author.

E-mail address: giulio.ruffini@neuroelectronics.com (G. Ruffini).

¹ Abbreviations used in the text: CSD: current source density, CSF: cerebrospinal fluid, EEG: electroencephalography, FC: functional connectivity, GM: grey matter, JR: Jansen-Rit model, LFP: local field potential, LaNMM: laminar neural mass model, MEG: magnetoencephalography, MUA: multiunit activity, NMM: neural mass model, PING: pyramidal interneuron gamma model, SEEG: stereotactic EEG, WM: white matter.

<https://doi.org/10.1016/j.neuroimage.2023.119938>.

Received 27 August 2022; Received in revised form 13 January 2023; Accepted 9 February 2023

Available online 11 February 2023.

1053-8119/© 2023 The Author(s). Published by Elsevier Inc. This is an open access article under the CC BY-NC-ND license

(<http://creativecommons.org/licenses/by-nc-nd/4.0/>)

patch-clamp experiments, adding further physical structure is necessary to contrast model outputs with electrophysiological recordings such as LFPs, stereotactic EEG (SEEG), or, in whole brain network models, scalp electro- or magnetoencephalography (EEG or MEG).

The raw outputs of NMMs are the membrane potential alterations induced by each synapse and the consequent firing rates of each population in the model. They are determined by a set of parameters describing, e.g., the dynamics of post-synaptic potentials, the relationship between membrane potential alteration and firing rate, population connectivity, and external inputs. Several studies have employed rodent multi-unit activity (MUA), LFP, and CSD measurements to estimate or fit some of these parameters (Blomquist et al., 2009; Lefebvre et al., 2009; Moran et al., 2008; Sotero et al., 2010). The average membrane potential or firing rate of the pyramidal populations is typically used to compare model outputs with MUA (Blomquist et al., 2009), LFP (Moran et al., 2008), or CSD (Lefebvre et al., 2009) measurements. Whole-brain computational studies use similar methods to simulate macroscopic electrophysiological recordings (e.g., EEG) in humans (Kunze et al., 2016; Merlet et al., 2013; Muldoon et al., 2016).

However, as discussed here, the connection between NMM membrane potential or firing rates with electrophysiology is a priori not well defined. Unlike detailed neuron compartment models (Hagen et al., 2018; Lee and Jones, 2013), the modeling framework in NMM studies does not use the physical laws of volume conduction (Poisson's equation) to predict measurements realistically beyond the dipole approximations that have been used to model EEG and even laminar measurements (Adams et al., 2022; Goodfellow, 2011; Pinotsis et al., 2017). In particular, in related work in Pinotsis et al. (2017), a multi-population NMM is embedded in the layers of the cortex using a dipole approximation by allocating each population to a single layer and by using the membrane potential as source of fields.

The first objective of this study is to create a framework for modeling cortical column physics by embedding NMMs more realistically in a physical medium. Since synaptic and associated return currents in pyramidal cells are the main LFP generators (Buzski et al., 2012; Nunez and Srinivasan, 2006), we will assign spatial coordinates to apical and basal dendrites of the pyramidal populations corresponding to the locations where the flow of ions across the membrane takes place. Then, using Poisson's equation (which governs the distribution of electrostatic potential in biological media) in a layered medium, we can realistically calculate the LFP profiles, bipolar LFPs, and CSD. We call this framework *laminar neural mass modeling*, or LaNMM for short, to emphasize its spatial and physical representation features. Our approach does not rely on the dipole approximation. In particular, we don't use the membrane potential as a proxy for the current generation as in previous work. Rather, we treat the synapses in pyramidal cells as monopolar current sources with return currents in other cell regions following biophysical principles. This is especially relevant for the simulation of LFPs, where the dipole approximation is inappropriate due to the proximity of sources and probes.

As the first application of this approach, we explore a LaNMM adapted to simulate fast (gamma band) and slow (alpha band) dynamics, and we fit the model parameters to simulate multi-contact LFP recordings collected from the prefrontal cortex (PFC) of two macaque monkeys performing a working memory task. This previously collected dataset is described in Bastos et al. (2018). There, it was found that LFP power in the gamma band (30–250 Hz) was strongest at superficial layers and in the low-frequency bands (4–22 Hz) at deep layers and that the phase and amplitude from deep low frequencies drove the phase and amplitude of superficial gamma dynamics.

These findings align with other studies of the visual cortex of non-human primates (Bollimunta et al., 2011; Buffalo et al., 2011; Johnston et al., 2019; van Kerkoerle et al., 2014; Maier et al., 2010; Spaak et al., 2012; Xing et al., 2012). However, the generality of these results has been recently questioned (Gieselmann and Thiele, 2022) since they may depend on the location of the recording site (e.g., visual vs. non-visual

cortex), the task/stimuli type, and the type of measurement employed (e.g., CSD vs. LFP). Bollimunta et al. (2008), using bipolar LFP and CSD measurements, found primary alpha power generators in the deep layers of the visual areas. However, in the inferior temporal gyrus (IT), alpha generators were located in superficial layers, and superficial to deep layer driving of alpha was found. Ninomiya et al. (2015), also using bipolar LFP and CSD measurements, replicated the findings of Bastos et al. (2018) Bastos et al. (2018) in visual areas but not in the Supplementary Eye Field area. Finally, Haegens et al. (2015) found maximal LFP alpha power in deep layers but a shift towards superficial layers using CSD. See Appendix A for a literature review summary of studies with different recording areas and measurement types.

A potential explanation for these discrepancies is that the LFP is calculated as the spatial line integral (along an arbitrary path) of the electric field from a (potentially remote) reference electrode to the recording site ($\Delta V = V_b - V_a = - \int_a^b \mathbf{E} \cdot d\mathbf{l}$, with the current density $\mathbf{J} = \sigma \mathbf{E}$). Thus, LFPs are strongly susceptible to selecting the reference point and currents potentially far from the measurement point. This can affect the power distribution and coupling measurements (e.g., Granger causality). Using the recorded data, we study the impact of the choice of reference or measurement type on the electrophysiological power profiles. Ultimately, it would be desirable to avoid the ambiguity induced by LFPs by estimating more local quantities such as bipolar LFP—approximated as the first spatial derivative of the voltage along the linear array, which removes the referencing ambiguity but not volume conduction confounds—or the CSD—approximated as the second spatial derivative of the voltage multiplied by the tissue conductivity, which deals with both problems. CSD analysis reveals the location, direction (inwards or outwards), and strength of the flow of ions and is widely used to calibrate the laminar location of recording sites (Bastos et al., 2018; Godlove et al., 2014; Maier et al., 2003). However, the derivatives (differences) computation can also decrease the signal-to-noise ratio.

Our second objective is to use our modeling framework to conduct model-driven data analysis and spatially disentangle the slow and fast activity sources. By adjusting model parameters such as pyramidal synapse locations, we can adjust the LFP, bipolar LFP, and CSD power profile distributions and voltage correlations across the PFC laminae and compare them with the recordings collected in macaque monkeys by Bastos et al. (2018). To define a quantitative loss function for parameter fitting while avoiding referencing issues, we use the complete set of bipolar voltage correlations as the simulation target to maximize the correlation with the multi-contact data. With this loss function, we deduce a family of laminar models composed of neuronal populations in superficial layers oscillating in the gamma band and in deep layers oscillating in the alpha band. The optimized architectures provide a mechanistic interpretation of the generation of slow and fast oscillations and approximate the measured LFP and CSD power profiles.

2. Methods

2.1. Multi-contact laminar recordings

The multi-contact dataset used in this study was collected in experiments described in Bastos et al. (2018). LFPs from the prefrontal cortex (ventrolateral prefrontal cortex and area 8a) of two macaque monkeys (*Macaca mulatta*) were recorded using a linear array of multi-contact laminar probes (16 contacts, 0.2 mm separation) while the animals were performing a search task (Fig. 1A and 1B). All surgical and animal care procedures were approved by the Massachusetts Institute of Technology (MIT) Committee on Animal Care and were conducted following the guidelines of the National Institute of Health and MIT's Department of Comparative Medicine. For our analysis, we selected the delay period (0.5–1s) of the successful memory encoding trials (see Appendix B for more details). The reference (ground) of the LFP recordings was located in the prefrontal cortex electrode chamber. To define which contacts belong to the superficial and deep layers, we aligned the electrode contacts

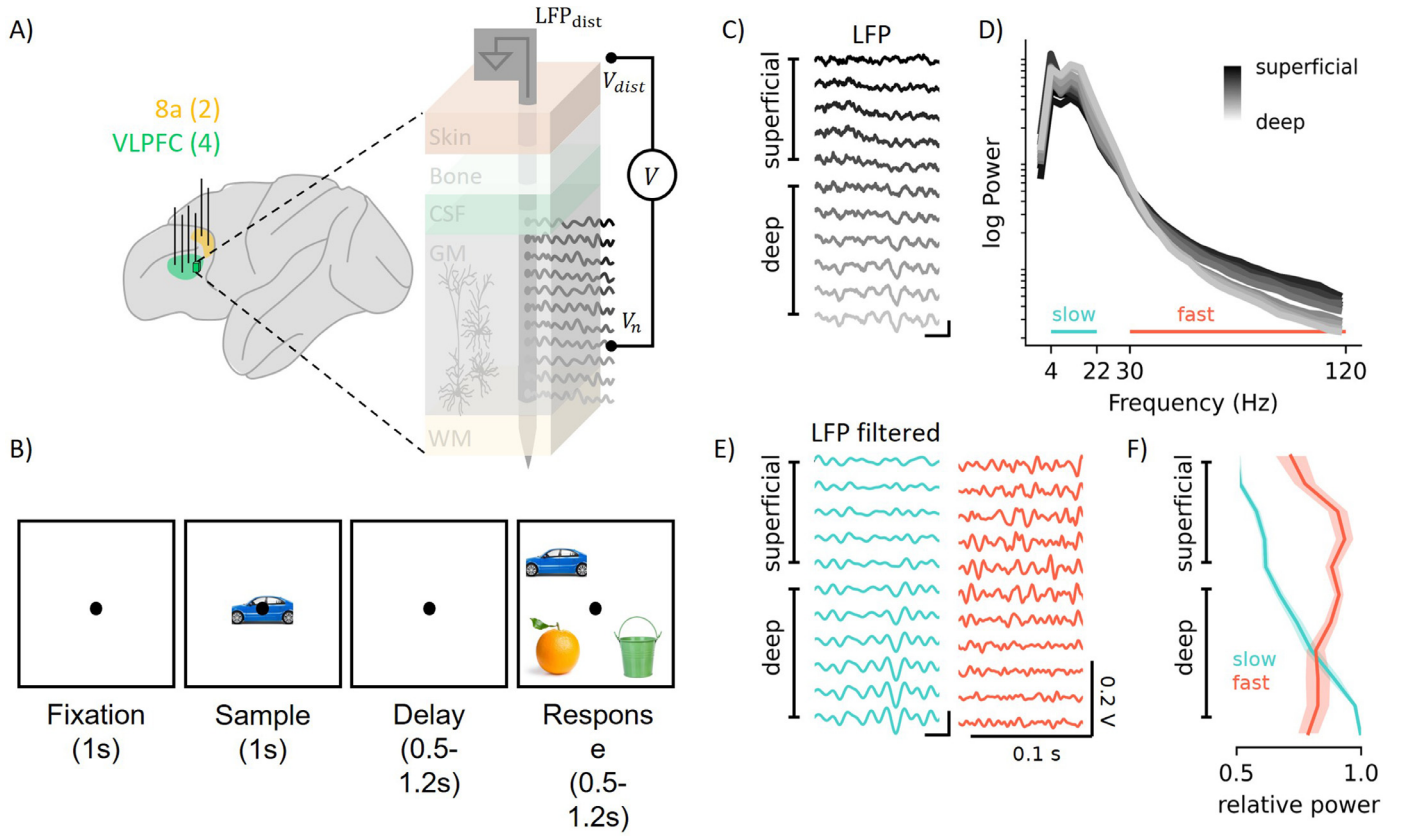


Fig. 1. A) Recordings from the ventrolateral prefrontal cortex (VLPFC) (4 electrodes) and area 8a (2 electrodes) referenced to the PFC electrode chamber. B) Schematic overview of the visual search task. The macaque had to make a saccade to the match after the delay period (0.5–1.2 s). C) Sample LFP (referenced to ground in electrode chamber) recordings during the delay period for one of the trials. D) Sample power spectrum across depth (gradient from superficial-black to deep-white contacts). E) Sample in A) was filtered in slow (4–22 Hz, blue) and fast (50–250 Hz) frequencies. F) Relative power across depth for the slow and fast frequencies. (For interpretation of the references to colour in this figure legend, the reader is referred to the web version of this article.)

where the cerebrospinal fluid (CSF) ends and the white matter (WM) begins. Our final selection included a total of 11 contacts spanning 2 mm of grey matter (GM), the first five contacts (0.8 mm) belonging to the superficial layers, and the rest in deep layers (1.2 mm), see Fig. 1(C) and Fig. 1(E) Bastos et al. (2018). The data is not openly available but can be reasonably requested through a data-sharing agreement with the corresponding author.

Fig. 1 (D) displays the power spectral density across the depth of the LFP data; there is a clear bump in slow frequencies (4–22 Hz), with a higher power in deep layers, and broadband gamma activity in fast frequencies (30–250 Hz, just until 120 Hz shown), with a higher power in superficial layers. We then filtered the data in these slow/fast frequency bands (Fig. 1E) and computed the relative power across depth (Fig. 1F). We found higher power in the fast band in superficial layers and the slow band in deep layers, as reported in Bastos et al. (2018) Bastos et al. (2018).

2.2. Synapse-driven formulation of NMM

Neural mass models (NMM) are mathematical representations of the dynamics of the average membrane potential and firing rate of a population of neurons in a cortical column (Lopes da Silva et al., 1976). In essence, a second-order differential equation describes the average membrane perturbation that a neuronal population m experiences at each synapse where it receives inputs from another population n . The synapse equation represents the conversion from an input presynaptic mean firing rate φ_n to a perturbation of the mean membrane potential $u_{m \leftarrow n}$ of the postsynaptic neuron population. We represent this relation here with the integral operator $\hat{L}_{m \leftarrow n}^{-1}$ (a linear temporal filter), the in-

verse of which is a differential operator $\hat{L}_{m \leftarrow n}$,

$$\begin{aligned} u_{m \leftarrow n}(t) &= \hat{L}_{m \leftarrow n}^{-1} [C_{m \leftarrow n} \varphi_n(t)] \\ \hat{L}_{m \leftarrow n} [u_{m \leftarrow n}(t)] &= C_{m \leftarrow n} \varphi_n(t) \end{aligned} \quad (1)$$

where $C_{m \leftarrow n}$ is the connectivity constant between the populations. The operator $\hat{L}_{m \leftarrow n}^{-1}$ can be expressed as a convolution of the input signal with a kernel of the form $h(t) = A \exp[-at]$ for $t > 0$ (Grimbert and Faugeras, 2006), and satisfies the Green's function equation $\hat{L}_{m \leftarrow n} [h(t - t')] = \delta(t - t')$ with appropriate causality boundary conditions, i.e.,

$$\hat{L}_{m \leftarrow n}^{-1} [f(t)] = \int_{-\infty}^{\infty} dt' h(t - t') f(t') \quad (2)$$

For simplicity, we will use single index notation (s) to represent the synapse from one neuronal population to another, such that the set of the synapse transmembrane potential perturbations is $\{s\} \equiv \{m \leftarrow n : C_{m \leftarrow n} \neq 0\}$.

The linear operator that describes the dynamics of synapse s is defined as

$$\hat{L}_s [u_s(t)] = \frac{1}{A_s} \left(\frac{1}{a_s} \frac{d^2}{dt^2} + 2 \frac{d}{dt} + a_s \right) u_s(t) \quad (3)$$

where A_s is the average excitatory/inhibitory synaptic gain and a_s is the rate constant of the synapse ($a_s = 1/\tau_s$, τ_s being the synaptic time constant).

Each neuronal population converts the sum v_m of the membrane perturbations from each of the incoming synapses or external perturbations to an output firing rate (φ_m) non-linearly by a sigmoid function,

$$v_m(t) = \sum_s u_s(t) \quad (4)$$

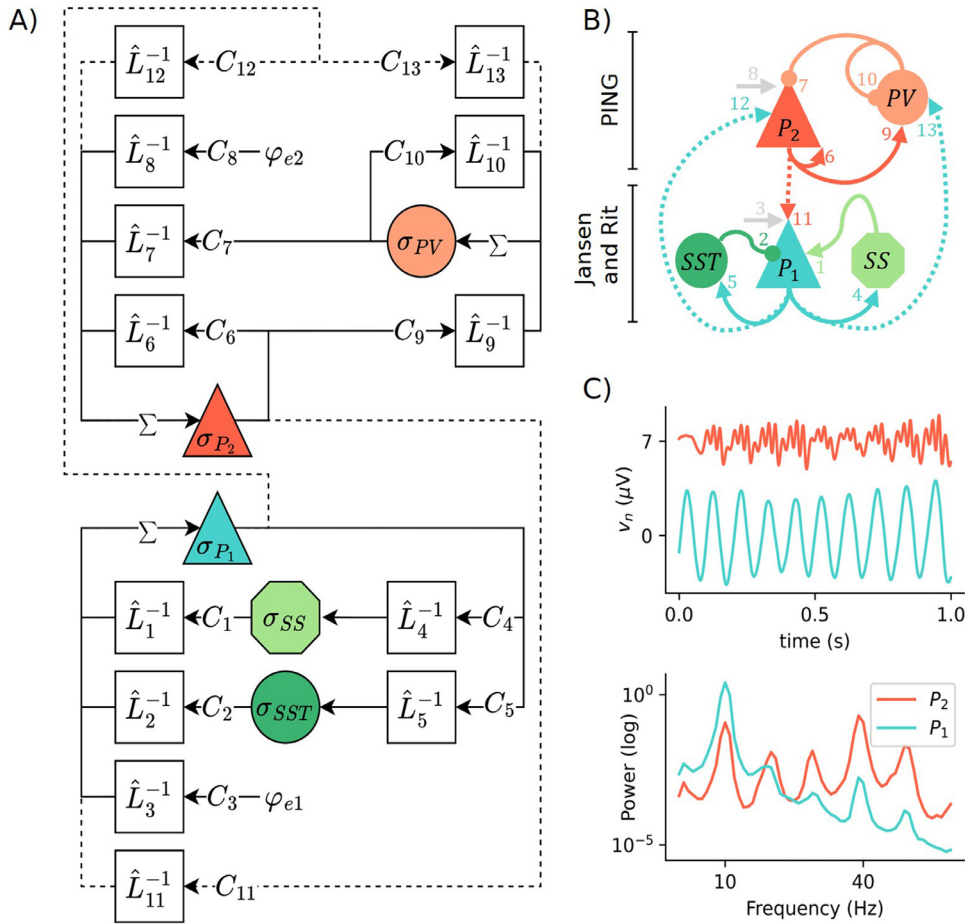


Fig. 2. A) Diagram of the model equations depicting the flow of information with synapse convolution operators, connectivity constants, summation of signals, and sigmoid functions. B) Illustration of the neuronal populations and the connectivity between them. Top, PING model, bottom, Jansen and Rit model. Rounded shapes in A) and B) represent inhibitory populations; the rest excitatory ones. C) Sample of the membrane potential of the Pyramidal populations (top) and their power spectral density (bottom).

$$\varphi_m(t) = \sigma_m(v_m(t)) = \frac{2\varphi_0}{1 + e^{r(v_0 - v_m(t))}} \quad (5)$$

where φ_0 is half of the maximum firing rate of each neuronal population, v_0 is the value of the potential when the firing rate is φ_0 and r determines the slope of the sigmoid at the central symmetry point (v_0, φ_0). We call this rewrite of the neural mass equations (Grimbert and Faugeras, 2006; Jansen and Rit, 1995) a synapse-driven formulation of an NMM. See Appendix C for more details.

2.3. Neural mass model

To generate the dynamics described in previous experimental studies (Bastos et al., 2018; Bonaiuto et al., 2018; Buffalo et al., 2011; Johnston et al., 2019; Maier et al., 2010; Ninomiya et al., 2015; Spaak et al., 2012), where the amplitude and phase of slow oscillations were observed to drive fast activity, we have combined two well-known NMMs. Slow oscillations in the alpha band (10 Hz) are produced by the Jansen and Rit model (Jansen and Rit, 1995), and fast oscillations in the gamma band (40 Hz) by a variation of the PING model (Borgers et al., 2008; Molaei-Ardekani et al., 2010).

The Jansen-Rit model (Fig. 2) consists of a population P_1 of pyramidal neurons, a population SS of excitatory cells (e.g., spiny stellate cells), and a population SST representing slow inhibitory interneurons (e.g., somatostatin-expressing cells, such as Martinotti cells). The PING model (Fig. 2) consists of two populations: a pyramidal population P_2 and a fast interneuron population PV (e.g., parvalbumin-positive cells, such as basket cells). The parameters of the Jansen and Rit model are maintained, so it oscillates at 10 Hz (in the Hopf Bifurcation) (Grimbert and Faugeras, 2006). The PING model has been manually modified, so it oscillates at 40 Hz (also in the Hopf bifurcation), so

it matches the dynamics of a fast circuit containing PV cells (Palop and Mucke, 2016). The connectivity between these models has been manually set so that there is a positive cross-frequency coupling and a negative power correlation from slow-to-fast frequencies, as is observed in experimental work (Bastos et al., 2018). Moreover, the connectivity profile is inspired by experimental and modeling studies characterizing fast and slow oscillations across the laminae (Jaramillo et al., 2019; Mejias et al., 2016) and the references therein.

The model equations are visually represented in Fig. 2A and described in detail, together with the parameters used, in Appendix D. Fig. 2C shows the membrane potential and power spectra of the two pyramidal populations of the model.

2.4. Physical environment

In the laminar framework, we embed the NMM into a physical medium composed of two isotropic media—GM and CSF. We assume that the GM layers have a uniform thickness across depth, from 0 to 2 mm. To produce electrophysiological measurements from the model, we assume that synapses to pyramidal cells are the main current generators, given the anatomy of these cells (an elongated form factor), organization (perpendicular to the grey matter surface), and temporal coherence (Buzski et al., 2012; Nunez and Srinivasan, 2006).

The apical and basal dendrites of the pyramidal populations, with locations across the vertical z -axis (Fig. 3A, z_l with layer $l \in [1, 6]$), provide the location of the input and output currents of each of the synapses (sinks and sources, respectively). For a detailed geometrical representation of the locations of the synapses with respect to the probe contacts across the GM see Fig. 3B. Since each synapse perturbation, u_s , has its location in space (z_l), it will produce a flow of ions across the membrane

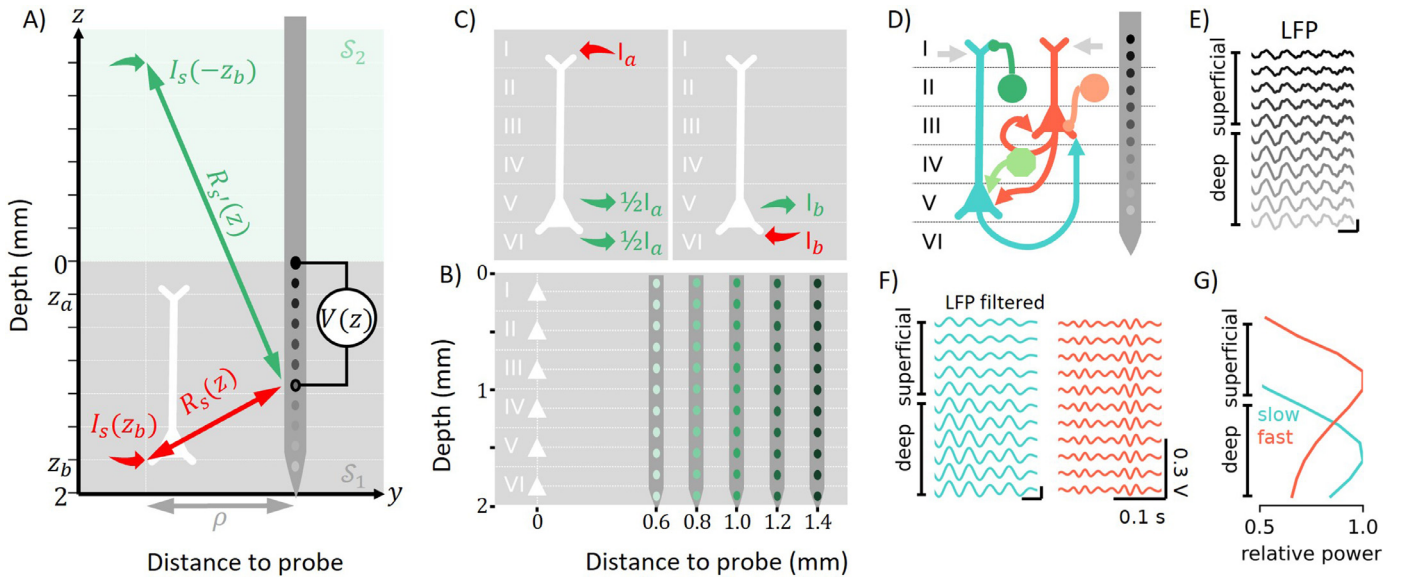


Fig. 3. Laminar framework. A) Schematic of the geometry used to simulate LFPs with a current source in a pyramidal cell shown with mirror source in CSF. B) Schematic of the locations of the sources in every layer and the probe contacts for the different distances to probe (ρ) in the grey matter (2 mm). C) Representation of the return currents in the model for an apical synapse (left) and a basal synapse (right). D) Example of a biologically informed architecture (only the synapses to pyramidal populations are shown for simplicity). E) Sample LFPs generated by the model with architecture in D) for a probe distance $\rho = 0.6$ mm. F) LFPs shown in E) filtered in slow and fast frequency bands. G) Relative power across depth for the LFPs shown in E) for the fast and slow frequency bands.

and therefore a synaptic current I_s . We assume that the membrane perturbation of a given synapse s , u_s , is linearly related to the injected current by a scaling factor that depends on the post-synaptic neuron population type and represents different aspects such as cell density and cell morphology. We capture this in a scaling factor—the *gain parameter* g_n —and write

$$I_s(z_l) = \begin{cases} g_n u_s(z_l), & \text{if } z_l \text{ is the location of } s \\ 0 & \text{otherwise} \end{cases} \quad (6)$$

For simplicity, the time variable t is omitted here and in the following equations.

In the model, each injected current is accompanied by a capacitive return current (charge conservation) supplied by charges accumulated in the membrane. The precise flow of this current depends on cell morphology and electrical properties and is a subject of the study (Mercadal et al., 2022). Based on previous studies Leski et al. (2011), here we assume that inputs to apical dendrites (layer location z_a) create a return CSD current at two locations on the basal dendrites, layer z_b and z_{b+1} , each with half the total current since there are large dendritic ramifications at the soma of pyramidal neurons (Fig. 3C). On the other hand, inputs to the basal dendrites (z_b) create a return current at the layer above (z_{b+1}). Thus, for each pyramidal cell, the total current generated at apical (I_a) and basal locations (I_b and I_{b+1}) is

$$\begin{aligned} I_a &= \sum_s I_s(z_a) \\ I_b &= \sum_s I_s(z_b) - \frac{1}{2} \sum_s I_s(z_a) \\ I_{b+1} &= -\sum_s I_s(z_b) - \frac{1}{2} \sum_s I_s(z_a) \end{aligned} \quad (7)$$

Once the current sources are specified, we can compute the electric potential and derived quantities. We model the potential field generated by each pyramidal cell by assuming there exist two isotropic media with conductivities $\sigma_1 = 0.40$ S/m (GM) and $\sigma_2 = 1.79$ S/m (CSF) (Miranda et al., 2013) and a common planar boundary (Fig. 3A). Then, the potential induced by a set of synaptic point current sources in GM

is Nunez and Srinivasan (2006)

$$V(z) = \frac{1}{4\pi\sigma_1} \sum_s \left[\frac{I_s(z_l)}{R_s(z)} + \left(\frac{\sigma_1 - \sigma_2}{\sigma_1 + \sigma_2} \right) \frac{I_s(z_l)}{R_{s'}(z)} \right] \quad (8)$$

Here, $R_s(z)$ and $R_{s'}(z)$ are the distances from the current source and mirror current source to the recording point (z), respectively (Fig. 3A). These distances depend on the parameter ρ , representing the distance from the point source to the probe. An example model of the LFP and its spectral properties is shown in Fig. 3D–G, for a sample architecture (3D) and for $\rho = 0.6$ mm.

The normal component of the electric field can be computed from the gradient of the potential. We can simulate the experimentally measured “normal component” of CSD (A/m³) from the electric potential using

$$\text{CSD}(z) = -\frac{\sigma}{(\delta z)^2} \left(V(z + \delta z) - 2V(z) + V(z - \delta z) \right) \quad (9)$$

where σ (S/m) is the tissue conductivity (Mitzdorf, 1985; Quairiaux et al., 2011). The values at the boundary layers are not evaluated.

2.5. Optimization function for model fitting

In order to compare the model and data and find optimal parameters, we computed the matrix of cross-contact correlations for the slow and fast frequency bands. The optimization process is represented in Fig. 4 and described hereafter.

Let V_a be the empirical filtered measurement at a contact a referenced to ground. We then create the list of all bipolar combinations

$$(\Delta_a)_i = (V)_i - V_a \quad (10)$$

To avoid redundancy, in what follows, $i > a$. Then, to get a generalized reference-free functional connectivity representation (FC) matrix between all pairs of bipolar channels in the data, we compute the two-point function

$$(\text{FC})_{ai,bj} = \langle (\Delta_a)_i (\Delta_b)_j \rangle \quad (11)$$

where the brackets denote the time average. Note that the two-point matrix FC includes as a subset the voltage power profiles referenced to any choice of the reference electrode.

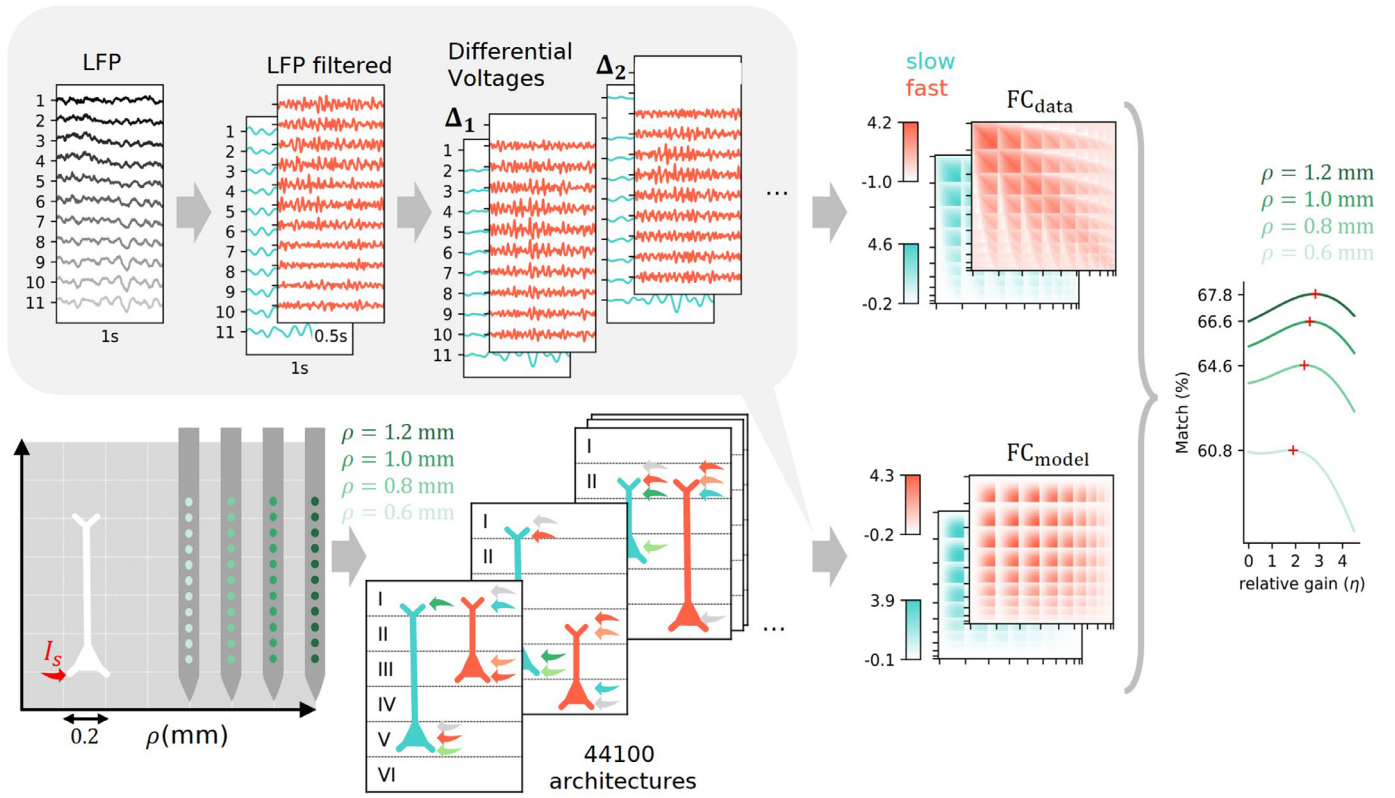


Fig. 4. Overview of the optimization process for model fitting. The shaded box (top-left) describes the process of transforming LFP data into the two-point function matrix, or functional connectivity matrix (FC, normalized by the standard deviation). To fit the model FC to the data, we optimized three different parameters: the distance to the probe ρ , the model architectures (a total of 44,100, just three samples represented at the bottom of the picture), and the relative gain η (just one sample fit from all the architectures is shown here). Each architecture specifies the location of each synapse to pyramidal cells in the model (across the six layers). FC matrices from data and from the model are compared (middle) and the parameters (architecture, distance to probe, and relative gain) for the best match are selected (right).

As with real data, we can produce the two-point matrix from our model, FC_{θ} , that will depend on the parameters θ . We select the best model parameters by maximizing the Pearson correlation coefficient (r) between the flattened data FC_{θ} and model FC matrices (only their diagonal and upper diagonal entries because they are symmetric) averaged over the two frequency bands, i.e., $\theta^* = \arg \max_{\theta} \chi(\theta)$ with

$$\chi(\theta) = \frac{1}{2} \left\{ r(FC_{\theta}^{slow}, FC_{data}^{slow}) + r(FC_{\theta}^{fast}, FC_{data}^{fast}) \right\} \quad (12)$$

The results discussed below are provided as the percent match between the model and data ($\chi(\theta) * 100$).

We adjusted the model using three sets of parameters (represented by θ): the distance to probe ρ , the model architecture, and the relative gain η between the slow and fast population. We explored 11 different ρ values, from 0.4 mm to 1.4 mm, with a size step of 0.1 mm (see Fig. 4, for simplicity, just four values are shown). We also explored all possible model architectures by varying the location of every synapse to the pyramidal populations (a binary choice of either apical or basal location) and, thus, the location and layer span of the pyramidal populations. Fig. 4 presents three examples of the different architectures. Each pyramidal population receives a total of 4 synapses to be assigned to one of six layers with the restriction that not all synapses in a population can be assigned to the same layer, so the analysis of combinations results in a total of $((6 \cdot 5/2)(2^4 - 2))^2 = 44,100$ possibilities. Here $6 \cdot 5/2$ is the number of possible apical/basal location pairs for a pyramidal cell population. At the same time, $2^4 - 2$ is the number of possible synapse assignments to each location, excluding the two cases where all the synapses are assigned to the same location (this ensures that a pyramidal population always spans two different locations). Finally, for each ρ and synaptic architecture choice, the relative gain factor between the slow and fast populations ($\eta = g_{P_1}/g_{P_2}$) was adjusted to maximize the opti-

mization function. The SciPy library method *optimize* (Virtanen et al., 2020) was used to fit the relative gain, after fixing the other two parameters (distance to probe and synapse connectivity architecture). Each simulation had a duration of 14 seconds and a sampling frequency of 1000 Hz. We fixed this duration because we observed that the model fit stabilized after about 12 seconds. We used in-house software from Neuroelectrics that is not openly available.

3. Results

3.1. Optimization results

We first need to adjust model parameters to assess the models ability to simulate the power profiles for different LFP-derived measurements. The optimization function for model fitting is a generalization of the power profiles, namely the covariance of arbitrary differential voltage measurements (the two-point functions derived from bipolar voltages, see Methods Section 2.5). We explored different model parameters to obtain the desired cross-correlation profiles.

The NMM parameters associated with intrinsic dynamics were fixed to produce representative fast (gamma) and slow (alpha) oscillations. We focused the fitting on laminar parameters directly influencing measurable quantities, namely the distance to probe (ρ), the location of the synapses (architectures), and the relative synaptic gain η (Fig. 4). The laminar architecture parameters specify not only the location of the synapses in the pyramidal cells (apical vs. basal) but also the location of the apical and basal dendrites across the layers (I-VI).

The family of models that best fit the data is described in Fig. 5. Fig. 5(A) displays the percentage match with real data for different distances to probe ρ and the architectures ordered from worst to best match

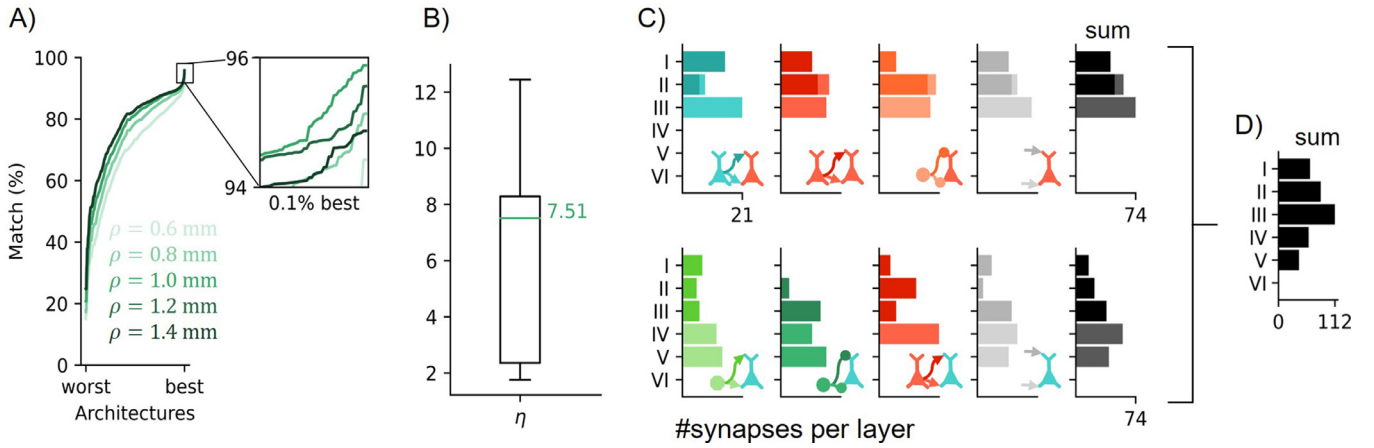


Fig. 5. Summary of optimization results. A) Percentage match with the real data for the different distances to probe ρ and all the 44,100 explored architectures ordered from worst to best. B) Box plot of the optimized relative gain η with the median of the distribution in green for the best 0.1% architectures of $\rho = 1.0$ mm. C) Histograms of the number of synapses per layer among the best 0.1% architectures for each connection in the model with $\rho = 1.0$ mm. Synapses to the fast population are shown on the top row, and synapses to the slow population are shown for reference in black. D) Sum over all the synapses for both slow and fast populations. (For interpretation of the references to colour in this figure legend, the reader is referred to the web version of this article.)

for an optimized relative gain (η). For most architectures, the best match happens with $\rho = 1.4$ mm, but if we zoom in to the 44 best architectures (0.1% of the total), we can see that the best fit happens with $\rho = 1.0$ mm. The model's fit to the data degrades for $\rho > 1.0$ mm. It is noteworthy that the optimization function does not flatten out near the optimum, so the best solutions are sharply defined.

The median relative gain of the 0.1% best architectures for $\rho = 1.0$ mm is 7.51, meaning that the gain of the fast circuit g_{p_2} is approximately seven times lower than the gain of the slow circuit g_{p_1} , $\eta = g_{p_1} / g_{p_2}$. This might be because the intrinsic power of gamma oscillations in our model is one order of magnitude higher than the power of alpha oscillations (Fig. 5B).

Then, we analyzed the resulting number of synapses per layer of the 0.1% best architectures (Fig. 5C) for $\rho = 1.0$ mm, and the optimized relative gain (Fig. 5B). For the fast circuit, most of the synapses appear located in the superficial layers I–III, whereas the synapses of the slow circuit span layers I–V. The synapses to the basal dendrites for the slow population are located in layers IV and V, and in the fast circuit, the majority happens in layer III. In Fig. 5(C) the peak synaptic activity for the slow population is always deeper than for the fast population. Although layer VI was included in the model, it was never the primary layer providing the synaptic currents in the top 0.1% of architectures.

3.2. Influence of the reference location in LFP measurements and model fit

To explore the effect of the electrical reference location on LFP measurements, we computed the LFP power profile using different electrical reference points: the ground in the prefrontal cortex chamber—a point distant to the sources (LFP_{dist})—and the first superficial contact in the gray matter (LFP_0). In order to mitigate the impact of possible far-field sources and referencing artifacts, we also evaluated the relative power of the fast and slow-frequency bands for the bipolar LFP and CSD measurements (Fig. 6A).

Given the definition of voltage as an integral of the field or currents and the results obtained from bipolar LFP and CSD measurements, we infer that the low-frequency LFP power data can be explained by currents generated by a long dipole spanning most of the cortex, with the high-frequency components generated by a shorter dipole in more superficial layers. Moreover, the LFP_0 profiles in superficial layers display a rapid increase in power with depth compared with deep layers, where it slowly plateaus, which differs from the LFP_{dist} case, where the profiles remain more stable across layers for the fast frequency band, probably

due to influences from more remote brain areas near the ground. This suggests that the spatial integral of the field along the vertical axis sums signals more coherently between the contacts in superficial layers than in deep layers, i.e., there is more spatial coherence of the electric field in superficial than deep layers. Moreover, the power peak of bipolar LFPs and CSD measurements also occurs in superficial layers.

We next computed the average relative power depth profile for the best 0.1% of architectures with $\rho = 1.0$ mm for each measurement (Fig. 6B). These models also predict the rapid increase in power in superficial layers for LFP_0 and the plateau in deep layers for both fast and slow frequencies. Furthermore, it shows a more superficial peak for the fast frequencies, as observed in the empirical data (Fig. 6A, LFP_0). The models also replicate the increased power in superficial layers for bipolar LFP and CSD. The estimated resulting density of synapses (Fig. 5D) is seen to reflect the associated CSD profiles from the model, with a peak in layer III (Fig. 6B, CSD).

The best solution is also shown in Fig. 6B (best fit), in dashed lines, and together with the FC_{data} used for the model fitting (Fig. 6C) as the best FC_{model} solution (Fig. 6D). We observe that the model fits the slow-frequency FC_{data} better than the fast-frequency FC_{data} . We also explored the power correlation and the modulation index of the model in Appendix E. We find similar patterns to those described in Bastos et al. (2018), namely a bottom-up coupling of phase and amplitude and anti-correlation of fast and slow-frequency power.

Altogether, we conclude from fitting the data that our model's main fast oscillatory synapses are located in superficial layers. This is consistent with the optimization results in Fig. 5C, where most synapses were present in superficial layers in the fast frequency sub-circuit. In the slow population model fit, the synapses are located in significantly lower layers than the fast ones. Moreover, they span across almost all layers, peaking in layer IV with considerable synapse activity also in layer V, which is absent from the fast population.

4. Discussion

4.1. The relative power distribution across layers depends on the choice of the measurement

In addition to the importance of taking into account the reference point when studying data in LFP space, Fig. 6(A) demonstrates that the distributions of the relative power vary significantly depending on the type of measurement. The CSD or bipolar LFP for the slow band

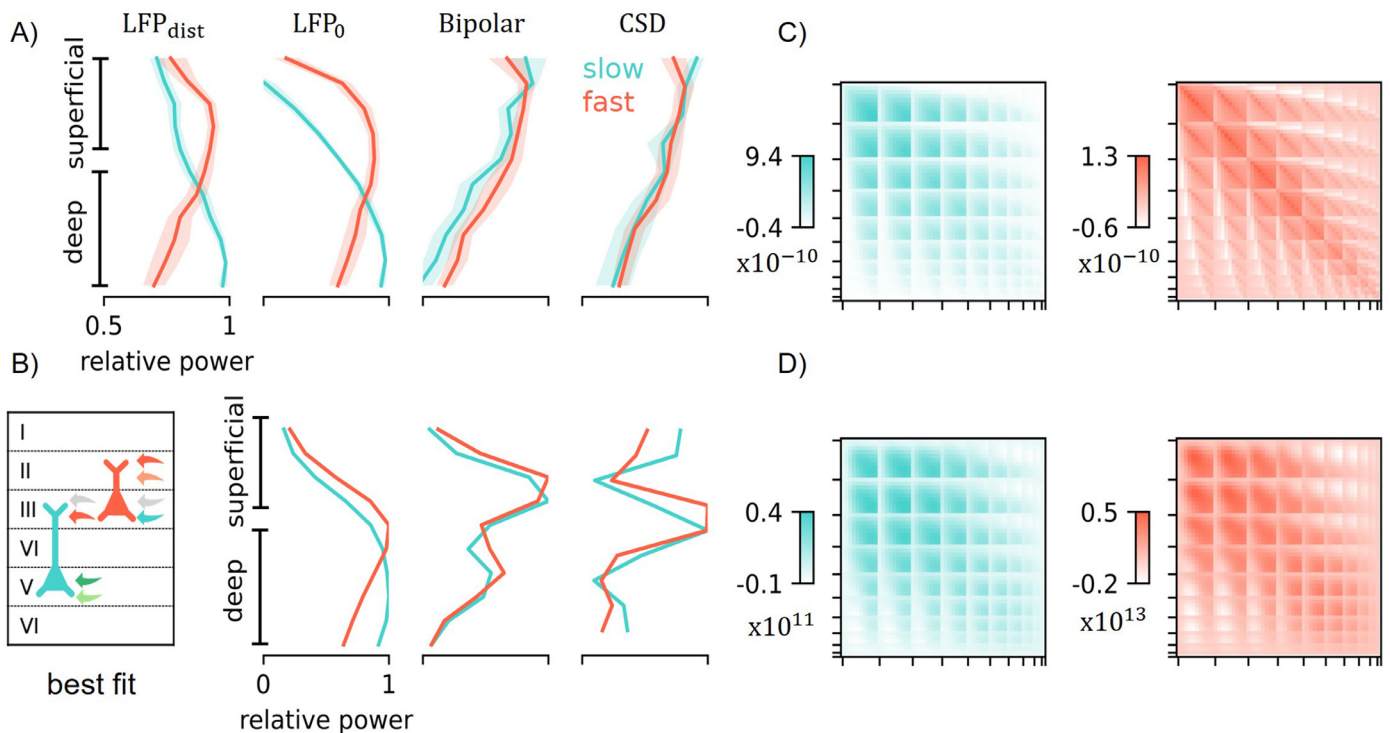


Fig. 6. Power profiles (left) and FC matrices for each frequency band (right, with the slow band in blue, fast in red) from experimental data (top) and from data generated by models (bottom). A) Relative power across depth for the real data. B) Average relative power across depth for the best 0.1% solutions (see Fig. 5). Each column displays the relative power profile for each measurement: LFP with a distant reference (LFP_{dist} , not available in the model), LFP with the reference in the first contact (LFP_0), bipolar LFP, and CSD. The dashed lines correspond to the relative power of the best fit (architecture shown in the bottom left). Filled areas show one standard error of the mean. C) FC of experimental data normalized by the standard deviation and D) normalized FC for synthetic data from best model fit, each separated into the slow and fast frequency bands. (For interpretation of the references to colour in this figure legend, the reader is referred to the web version of this article.)

peak shifts to superficial layers compared to voltage profiles, in agreement with other existing studies (Bollimunta et al., 2011; Haegens et al., 2015). We note that most studies that find the peak of slow oscillations in deep layers are based on monopolar LFP voltage recordings (LFP_{dist} here), with a remote reference far from the electrode contacts (Bastos et al., 2018; Buffalo et al., 2011; van Kerkoerle et al., 2014; Maier et al., 2010; Smith et al., 2013).

The referencing issue can, in part, be addressed by re-referencing the data to local electrode contacts (Haegens et al., 2015; van Kerkoerle et al., 2014; Ninomiya et al., 2015). It can be further mitigated using bipolar measurements (bipolar LFP, related to the local electric field and current density) or CSD estimates. Unlike CSD measurements, monopolar measurements (LFP) and bipolar LFPs are susceptible to volume conduction from remote sources since they are calculated as the spatial integral of the electric field between the measurement and reference point. It is critical to consider more local types of measurements, such as the bipolar LFP or CSD, to gain more information about the synaptic currents underlying LFP measurements (Bollimunta et al., 2008; Haegens et al., 2015; Hagen et al., 2018) (see Fig. A.1).

It is important to note that other factors may influence the power profiles across layers: recording area (Bollimunta et al., 2008; Haegens et al., 2015; Ninomiya et al., 2015), experimental task (Bollimunta et al., 2011; Gieselmann and Thiele, 2022; Haegens et al., 2015; Johnston et al., 2019; van Kerkoerle et al., 2014), and experimental procedures such as electrode placement (Ninomiya et al., 2015). The proper identification of the transition between superficial and deep layers, which should also depend on the area recorded (Buffalo et al., 2011; Godlove et al., 2014; Ninomiya et al., 2015), can also be confounding across studies. Future work should consider all these factors while trying to establish a golden standard for the experimental procedures (as suggested in (Ninomiya et al., 2015)). The current availability of massively dense

depth probe electrodes should shed light on these issues in the coming years.

4.2. Mesoscale laminar models can predict physical measurements of cortical rhythms across the laminae

A model-driven interpretation of the role of synaptic currents can shed some light on disagreements in the literature concerning the location of oscillatory generators. In addition to measurement issues related to referencing, confusion may arise from terminology—“generator” is a loose term that a physical modeling approach can clarify. Because electrophysiological recordings are driven by synaptic currents which may be distant from the projecting or receiving cell bodies, there is a disassociation between soma location and generation locus. Thus, in this paper, we associate the term generators with synapses and the currents they generate.

In this study, we showed that our modeling framework could produce different oscillatory rhythms across layers and different types of laminar measurements extracted from multi-contact electrodes in a physically realistic manner (Fig. 6). Despite the caveats listed in Section 4.1, it is interesting to note that we found the laminar generators for the slow rhythm to be located in significantly deeper layers than the generators of the fast rhythm. Indeed, the top-performing models for the fast (gamma) frequency synaptic generators included exclusively superficial layers 1–3. In contrast, the top performing models for the synaptic generators of the slower (alpha) frequency included deeper layers 4 and 5, and had a smaller presence also on superficial layers. This suggests that the generating circuit for the slow oscillations integrates information across a larger spatial extent and samples from all layers.

4.3. Relation of the current model to current theories of slow and fast oscillations

Our observation of superficial layers for gamma generation, and superficial and deep layers for alpha generation fits nicely with previous proposals of the role of these oscillations in the cortex. Slow frequencies (e.g., alpha) have been implicated in feedback processes and gamma in feedforward sensory processing (Bastos et al., 2015; Miller et al., 2018). Generally, top-down anatomical projections, achieved through feedback connections, derive mostly from deep cortical layers, and bottom-up anatomical projections, achieved by feedforward connections, derive most strongly from superficial layers (Markov et al., 2013). Bottom-up sensory processing is thought to rely on point-to-point connectivity and driving connections which determine the receptive field properties of downstream neurons (Sherman and Guillery, 1998). Consistent with a bottom-up process, our model suggests that the gamma oscillatory circuit is largely constrained to the layers that send feedforward output (layers 2/3). Top-down processing is thought to rely on more modulatory, non-linear connections which integrate multiple streams of information (Bastos et al., 2012). Consistent with a more integrative, top-down process, our modeling results suggest that slow oscillations are generated by a more complex and spatially distributed process that may combine anatomical feedforward and feedback connections.

4.4. Limitations

We discuss next the limitations of the framework we propose in this study. First, our modeling approach is based on the concept of neural mass models, which are not in general mean field theories derivable from first principles (i.e., derivable as statistical aggregates of microscale models) (Clusella et al., 2022; Deschle et al., 2020; Faugeras et al., 2009). The direct extension of our framework to include so-called next-generation neural mass models (Clusella et al., 2022; Montbrió et al., 2015) can address this limitation. Second, we assume that the currents in each population are generated by cells in roughly the same cortical locations (at layer scale) so as not to affect too much the lead field approximation used to estimate voltages at the probe location. This could be addressed by computing the lead fields from current sources using distributions of source neurons (as in Mercadal et al. (2022)) under some assumptions of statistical independence of the electrical and dynamical features of the model. Third, to estimate the voltage of the cortical column model (Eq. 8), we assume the column can be represented as a set of monopoles and that the measurement point is relatively far from it. In reality, there is a field of sources (Buzski et al., 2012) in the cortical surface/patch, and the measurement contact is embedded in it. Moreover, our modeling framework focuses on the main understood current sources, but other ones may play a role in the generation of LFPs (e.g., back propagating action potentials) (Pinotsis et al., 2017). More realistic modeling approaches can be explored, such as using as large set of multiple neuron compartment models as sources distributed in a layer with embedded electrodes (Mercadal et al., 2022). Additionally, in our estimations of CSD (model and data), we assume as is often done in experimental work using depth probes that all currents occur in the vertical plane. To properly extract the CSD, we would need measurements in 3D space. However, this assumption is reasonable given that pyramidal cells are mostly homogeneously oriented perpendicular to the surface (Buzski et al., 2012; Nunez and Srinivasan, 2006).

Another limitation of this work is the relative simplicity of the presented NMM, with just two pyramidal populations oscillating in alpha and gamma bands, respectively. However, this simple model architecture inspired by the experimental work of Bastos et al. (2018) has allowed us to explore all combinations of pyramidal synapse locations. Moreover, even though the model allows for synapses in layer IV, there is no model of thalamic input nor a granular population model (which would be at alpha or lower frequencies). We justify this by the desired simplicity of the model and by the fact that the data we model belongs

to the delay period of a working memory task, where the thalamic input is not expected to be strongly present. Finally, our LaNMM has been implemented with only two synapse locations (apical and basal dendrites) per pyramidal cell. Recent work has addressed this limitation along with improving the model of return currents (Mercadal et al., 2022), which is also a simplified model in the present work.

There are also limitations with respect to the choice of parameters to optimize and the selected feature to fit. Among all the potential parameters in the LaNMM formalism, we choose to fit the ones that belong to the new framework (e.g., synapse location) instead of the usual ones of an NMM formalism (e.g., synaptic constants or connectivity constants). The reason for this selection is that we wanted to maintain the dynamical behavior (alpha/gamma oscillations), and just focus on the location across space (e.g., depth and distance from the probe) of the oscillatory generators. A higher resolution used in all fitted parameters could be explored in future work, as well as fitting more parameters, e.g., using Variational Inference techniques (Pinotsis et al., 2017). For example, the limitation in synapse locations (with only six possible values) could be relaxed in the future, which would be appropriate to fit higher-resolution multiprobe data. Moreover, other features to focus on and fit could be explored, such as those deriving from signal morphology, e.e., cycle-by-cycle analysis (Cole and Voytek, 2019). This may be very challenging, as the location of synapses relative to the probe has a huge impact on the shape of the signals, as we discuss elsewhere (Lopez-Sola et al., 2022; Mercadal et al., 2022). We chose the two-point matrix FC as a feature for fit since it treats each contact in the same way while including as a subset the voltage power profiles referenced to any choice of the reference electrode, avoiding any possible volume conduction and referencing biases.

5. Conclusions

In this study, we first extend the neural mass modeling formalism to include multiple oscillatory circuits and simulate realistic electrophysiological signals. We then use it to analyze data collected from multi-contact laminar measurements in the macaque. The analysis is performed with a simple laminar model whose connections are derived from literature and that is designed to produce coupled fast and slow oscillatory activity. We fit model parameters and the location of synapses by matching voltage statistics in the slow and fast frequency bands, leading to a solution with slow frequency oscillations generated by synapses spanning most cortical layers and fast oscillations in superficial layers. The laminar modeling framework developed here can help understand the neural mechanisms of electrophysiological signals and shed some light on controversial issues regarding discrepancies in LFP, bipolar LFP, and CSD measurements. The modeling framework may also help establish a firmer connection between neural mass models and EEG/MEG data and can be easily extended to analyze future data collected with dense probes. Finally, the possibility of modeling both slow and fast oscillatory activity within the same computational framework opens the possibility of understanding the origin of generalized EEG slowing observed in neurodegenerative conditions such as Alzheimers Disease and dementia, where slowing of alpha and reduced power of gamma activity are observed with disease onset and progression Benwell et al. (2020).

Declaration of Competing Interest

Roser Sanchez-Todo, Edmundo Lopez-Sola, and Borja Mercadal work at Neuroelectrics, a company developing brain stimulation solutions. Giulio Ruffini works at and is a co-founder of Neuroelectrics.

Credit authorship contribution statement

Roser Sanchez-Todo: Conceptualization, Methodology, Software, Validation, Data curation, Writing – original draft, Visualization.

André M. Bastos: Methodology, Resources, Data curation, Conceptualization, Writing – review & editing. **Edmundo Lopez-Sola:** Software, Writing – review & editing. **Borja Mercadal:** Conceptualization, Methodology. **Emiliano Santarnecchi:** Conceptualization, Methodology. **Earl K. Miller:** Writing – review & editing. **Gustavo Deco:** Supervision, Writing – review & editing. **Giulio Ruffini:** Conceptualization, Methodology, Formal analysis, Writing – original draft, Supervision, Project administration.

Data availability

Data will be made available on request.

Acknowledgement

This work was supported under European Unions Horizon 2020 research and innovation programme under grant agreement No 101017716 (Neurotwin) and by the European Research Council (ERC

Synergy Galvani) under the European Unions Horizon 2020 research and innovation programme (grant agreement No 855109). NIMH 1R01MH131715-01, Office of Naval Research N00014-22-1-2453, The JPB Foundation, NIMH R00MH116100, R01 AG060981-01, ADFF-FTD GA201902–2017902 The authors wish to thank Esteban Féliz and Kyra Kadhim for revising the document, and Fabrice Wendling for useful discussions.

Appendix A. Literature review

Fig. A.1 provides a graphical summary of the literature review performed of the different measurement types (rows) used in this study. It also shows the different results obtained for the different areas recorded. When using LFPs without considering reference location, most studies conclude that the fast activity is in the upper layers and slow activity is in the lower layers. The conclusions change with other, more local measurement types (bLFPs and CSD).

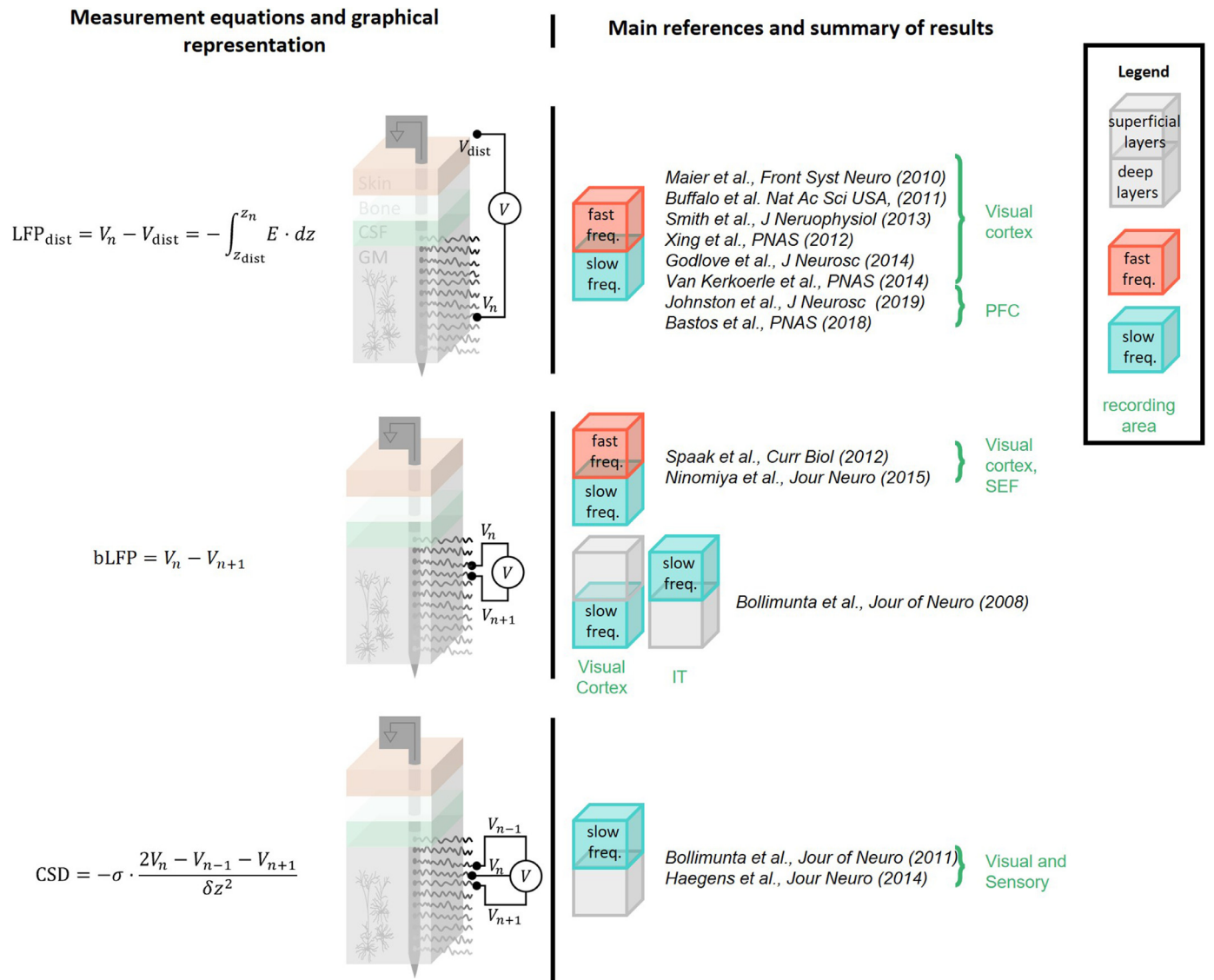


Fig. A.1. Summary of literature review of the slow and fast cortical generators. Each row represents a different measurement type, from top to bottom: distant LFPs (LFP_{dist}), bipolar LFPs (bLFP), and CSD. On the left of each row, the respective measurement equations and a graphical representation is shown. On the right, a graphical representation of where the slow and fast oscillations are situated (superficial or deep layers) and the main references. The text in green denotes the recording site. (For interpretation of the references to colour in this figure legend, the reader is referred to the web version of this article.)

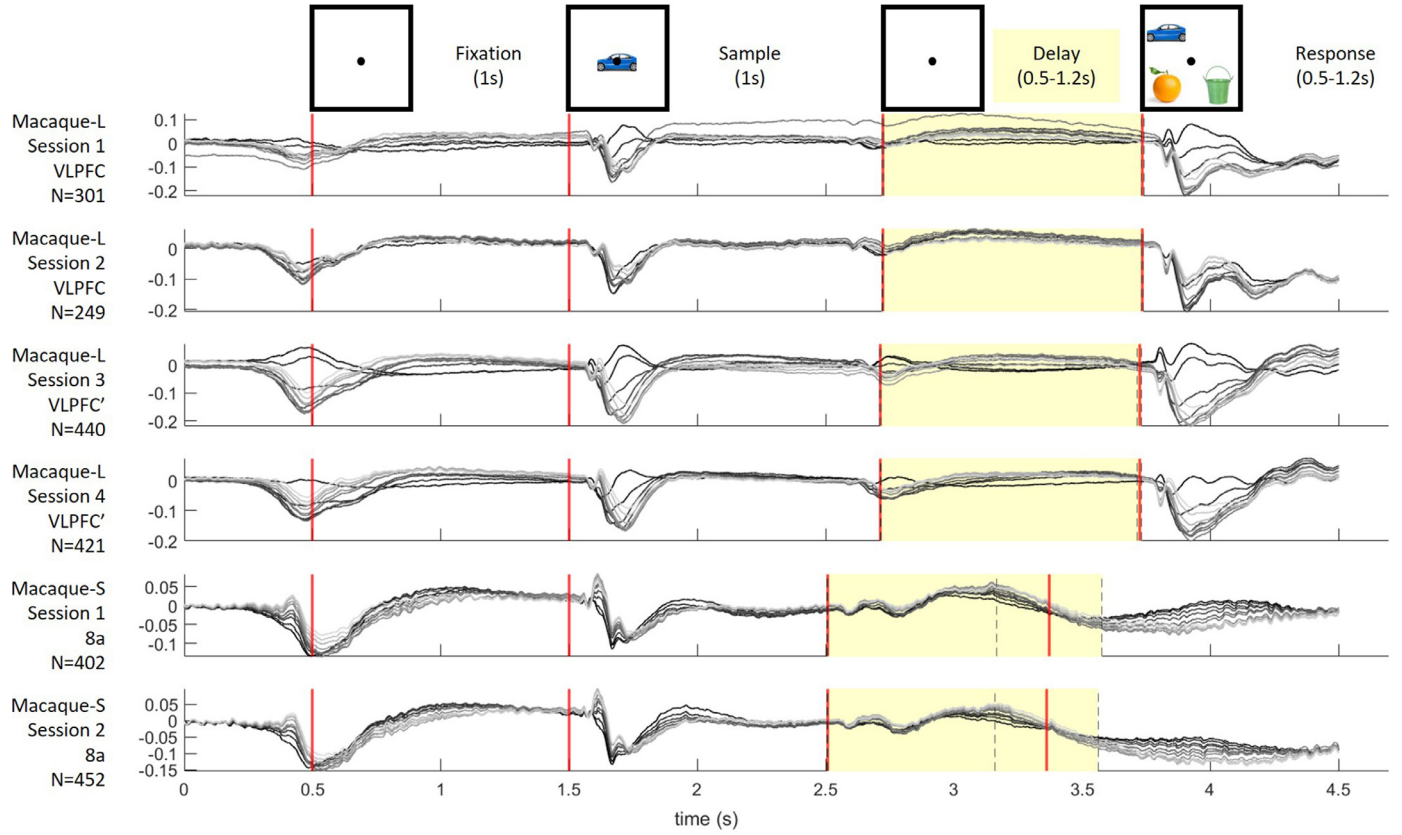


Fig. B.1. Average LFPs across trials, N, for the different monkeys and different sessions. The delay period is in between the 'sampleOff' and 'testOn' marks, in pink, which varies in time for monkey S (mean shown for the 'testOn', the standard deviation in dashed lines). Each trace represents a different contact.

Appendix B. LFP data analysis

The multi-contact dataset used in this study was collected in experiments described in [Bastos et al. \(2018\)](#). We analyzed the data from 2 monkeys (L, S, male, and female, respectively) for six different sessions and two different brain areas (VLPFC and 8a). In [Fig. B.1](#), the average across the correct trials for each session is shown. The delay period of monkey-L was fixed (1s), but for monkey-S, it varied from 0.5 s to 1 s.

Appendix C. Jansen and Rit model in synapse-driven formulation

C1. Jansen and Rit model description

In 1993, [Jansen et al. \(1993\)](#) developed a model of a cortical column which consists of three different neural populations: pyramidal neurons (P), inhibitory interneurons (I) and excitatory interneurons (E). The state variables of the model are the membrane potential and the firing rate of the neuron populations, and they are linked by two different transformations that shape the classical properties of neurons: the pulse-to-wave $h(t)$ and wave-to-pulse $\sigma(v)$ functions ([Ahmadizadeh et al., 2018](#); [Grimbert and Faugeras, 2006](#)).

The $\sigma(v)$ operator, also called “wave-to-pulse”, introduces a nonlinear component that transforms the average membrane potential of a population $v(t)$ (mV) into an average firing rate $\varphi(t)$ (Hz)

$$\varphi(t) = \sigma(v(t)) = \frac{2\varphi_0}{1 + e^{r(v_0 - v(t))}} \quad (\text{C.1})$$

where φ_0 is half of the maximum firing rate of each neuronal population, v_0 is the value of the potential when the firing rate is φ_0 and r determines the slope of the sigmoid at the central symmetry point (v_0, φ_0). See [Table C.1](#) for the standard parameter values of the model equations.

The $h(t)$ operator, also called “pulse-to-wave”, converts the average rate of action potentials into an average post-synaptic potential, either excitatory $h_{0,1}(t)$ or inhibitory $h_2(t)$. The transformation is done by a second-order linear differential operator whose impulse response is given by

$$h(t) = \begin{cases} aA te^{-t} & t \geq 0 \\ 0 & t < 0 \end{cases} \quad (\text{C.2})$$

where A is the synaptic gain (in potential units, e.g., mV) and a (with units of time, s^{-1}) is the rate constant (and its reciprocal τ the time constant) of the synapse. Each of these post-synaptic boxes corresponds to solving a differential equation of the form

$$\ddot{u}(t) + a\dot{u}(t) + a^2u(t) = aA\varphi(t) \quad (\text{C.3})$$

where $\varphi(t)$ is the output of the sigmoid function (average firing rate of a population, in Hz) and $u(t)$ is the membrane potential alteration in each of the synapses. The function $h(t)$ is the equation's Green's function or impulse response, i.e., the solution with $\varphi = \delta(t)$ and appropriate boundary conditions. The parameters A and $\tau = 1/a$ represent the maximal amplitude of excitatory or inhibitory post-synaptic potential and the average time constant for each synapse type, respectively.

This second-order differential equation can be decomposed in a system of two equations,

$$\begin{aligned} \dot{u}(t) &= z(t) \\ \dot{z}(t) &= aA\varphi(t) - 2az(t) - a^2u(t) \end{aligned} \quad (\text{C.4})$$

There are thus three main state variables in the model: the average membrane potential of each of the subpopulations of the system: $v_P(t)$ for the pyramidal cells, and $v_E(t)$, $v_I(t)$ for the excitatory and inhibitory interneurons, respectively. The average membrane potential v_P of the pyramidal population has been typically used as a proxy source of electrophysiological signals such as LFPs and EEG (dipole generator). We

Table C.1

Parameters, description, and standard values of the JR synapse model. Values taken from [Jansen and Rit \(1995\)](#). Note that the sigmoid parameters in this model (v_0, φ_0, r) are common to all neuron populations.

Parameter	Description	Value
A_s	Average excitatory and inhibitory synaptic gain	$A_{1,3,4,5} = 3.25 \text{ mV}$ $A_2 = -22 \text{ mV}$
a_s	Time rate constant of average excitatory and inhibitory postsynaptic potentials	$a_{1,3,4,5} = 100 \text{ s}^{-1}$ $a_2 = 50 \text{ s}^{-1}$
C_s	Average number of synaptic contacts between population types	$C_1 = 108$ $C_2 = 33.7$ $C_3 = 1$ $C_4 = 135$ $C_5 = 33.75$
v_0	Potential when 50% of the firing rate is achieved	6 mV
φ_0	Half of the maximum firing rate	2.5 Hz
r	Slope of the sigmoid function at v_0	0.56 mV^{-1}

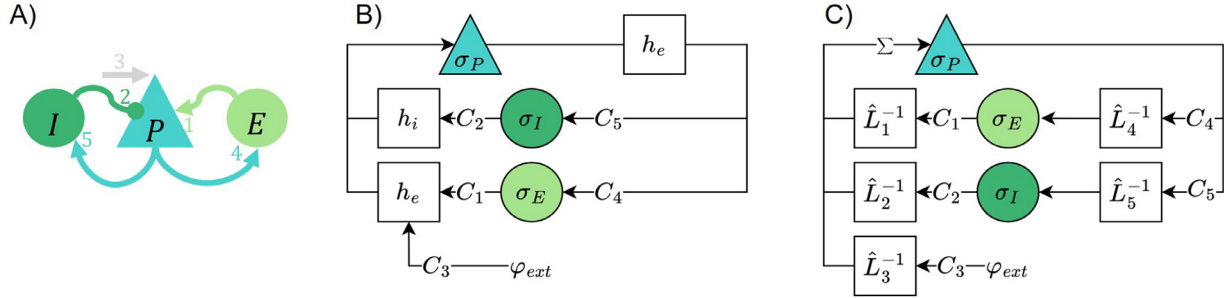


Fig. C.1. Jansen and Rit model. A) Schematics of the connections between the different populations: P—Pyramidal, I—Inhibitory interneuron and E—Excitatory interneuron. B) simplified wired diagram exploiting the presence of common synapse types, C) full synapse-driven wiring diagram with all synapses explicitly represented.

improved upon this first-order approximation in the LaNMM framework (see next section).

The Jansen and Rit model can be described with a set of six differential equations with each pair corresponding to a population,

$$\begin{aligned}
 \dot{u}_0(t) &= u_3(t) \\
 \dot{u}_3(t) &= a_0 A_0 \left[\sigma_P(u_1(t) - u_2(t)) \right] - 2a_0 u_3(t) - a_0^2 u_0(t) \\
 \dot{u}_1(t) &= u_4(t) \\
 \dot{u}_4(t) &= a_1 A_1 \left[\varphi_{ext}(t) + C_2 \sigma_E(C_1 u_0(t)) \right] - 2a_1 u_4(t) - a_1^2 u_1(t) \\
 \dot{u}_2(t) &= u_5(t) \\
 \dot{u}_5(t) &= a_2 A_2 \left[C_4 \sigma_I(C_3 u_0(t)) \right] - 2a_2 u_5(t) - a_2^2 u_2(t)
 \end{aligned} \quad (C.5)$$

For an illustrative description of the model equations see [Fig. C.1 A\)](#) and B). In this cortical column configuration, the membrane potential of the pyramidal population is $v_P(t) = u_1(t) - u_2(t)$, the membrane potential of the inhibitory interneuron population is $v_I = u_0$ and of the excitatory interneuron population is $v_E = u_0$.

C2. Derivation of the synapse-driven formulation from Jansen and Rit equations

We can rewrite the Jansen and Rit NMM focusing on the dynamics of each of the synapses independently, allowing us to generalize the equations and simplify the definition of the neural dynamics to develop more complex models. We will define a new linear operator, $\hat{L}^{-1}[\cdot]$, to transform the pre-synaptic average firing rate of neuron n φ_n into a post-synaptic membrane perturbation of neuron m $u_{m \leftarrow n}$:

$$\begin{aligned}
 u_{m \leftarrow n}(t) &= \hat{L}_{m \leftarrow n}^{-1} [C_{m \leftarrow n} \varphi_n(t)] \\
 \hat{L}_{m \leftarrow n} [u_{m \leftarrow n}(t)] &= C_{m \leftarrow n} \varphi_n(t)
 \end{aligned} \quad (C.6)$$

The inverse of the $\hat{L}(\cdot)$ operator and can be expressed as an integral (convolution) operator using the typical $h(t)$ kernel,

$$\hat{L}^{-1}[f(t)] = \int_{-\infty}^{\infty} dt' h(t - t') f(t') \quad (C.7)$$

Note that, for simplicity, the index s will represent the synapse from one neuronal population to another $m \leftarrow n$, where $n, m \in [P, E, I, ext]$ and

$(m, n): C_{m \leftarrow n} \neq 0$. Then, we can define the linear operator that captures the synapse dynamics $\hat{L}_s(\cdot)$ as

$$\hat{L}_s[u_s(t)] = \frac{1}{A_s} \left(\frac{1}{a_s} \frac{d^2}{dt^2} + 2 \frac{d}{dt} + a_s \right) u_s(t) \quad (C.8)$$

The sum of each pre-synaptic perturbation into neuron n is the overall membrane potential perturbation of the post-synaptic neuron, v_m ,

$$v_m(t) = \sum_s u_s(t) \quad (C.9)$$

and the average firing rate of the neural population, φ_m , is the output of the non-linear function,

$$\begin{aligned}
 \varphi_m(t) &= \sigma_m(v_m(t)) \\
 \sigma_m(v_m(t)) &= \frac{2\varphi_0}{1 + e^{r(v_0 - v_m(t))}}
 \end{aligned} \quad (C.10)$$

Finally, the set of equations, one for each synapse (m, n) and neuron m ,

$$\begin{aligned}
 u_{m \leftarrow n}(t) &= \hat{L}_{m \leftarrow n}^{-1} [C_{m \leftarrow n} \varphi_n(t)] \\
 v_m(t) &= \sum_{n: C_{m \leftarrow n} \neq 0} u_{m \leftarrow n}(t) \\
 \varphi_m(t) &= \sigma_m(v_m(t))
 \end{aligned} \quad (C.11)$$

which we call the synapse-driven reformulation of the Jansen-Rit that can be easily be extended to other, more complex NMMs.

Rewritten using the synapse-driven formalism, the Jansen and Rit equations specify the dynamics as a function of the average firing rate for each neuronal population φ_n , the average membrane potential for each population v_n , and the membrane perturbation per each synapse u_s ,

$$\begin{aligned}
 \hat{L}_1[u_1(t)] &= C_1 \varphi_P = C_1 \sigma_P(v_P) = C_1 \sigma(u_2(t) + u_5(t) + u_4(t)) \\
 \hat{L}_2[u_2(t)] &= C_2 \varphi_E = C_2 \sigma(v_E) = C_2 \sigma(u_1(t)) \\
 \hat{L}_3[u_3(t)] &= C_3 \varphi_P = C_3 \sigma(v_P) = C_3 \sigma(u_2(t) + u_5(t) + u_4(t)) \\
 \hat{L}_4[u_4(t)] &= C_4 \varphi_I = C_4 \sigma(v_I) = C_4 \sigma(u_3(t)) \\
 \hat{L}_5[u_5(t)] &= C_5 \varphi_{ext}(t)
 \end{aligned} \quad (C.12)$$

Fig. C.1 C) provides the diagram and dynamics of the Jansen and Rit NMM in the Synapse-driven implementation.

Table D.1

Parameters, description, and standard values of the model. Values are taken from Jansen and Rit (1995) and Molaee-Ardekani et al. (2010). Note that the sigmoid parameters in this model (v_0, φ_0, r) are common to all neuron populations. Moreover, excitatory synapses have the same synapse dynamics, $(A, a)_{AMPA} = (A, a)_{1,3,4,5,6,8,9,11,12,13}$, and inhibitory synapses have either fast dynamics, $(A, a)_{GABA_{fast}} = (A, a)_{7,10}$, or slow, $(A, a)_{GABA_{slow}} = (A, a)_2$.

Parameter	Description	Value
A_s	Average excitatory and inhibitory synaptic gain	$A_{AMPA} = 3.25 \text{ mV}$ $A_{GABA_{slow}} = -22 \text{ mV}$ $A_{GABA_{fast}} = -30 \text{ mV}$
a_s	Time rate constant of average excitatory and inhibitory postsynaptic potentials	$a_{AMPA} = 100 \text{ s}^{-1}$ $a_{GABA_{slow}} = 50 \text{ s}^{-1}$ $a_{GABA_{fast}} = 220 \text{ s}^{-1}$
C_s	Average number of synaptic contacts between population types	$C_1 = 108, C_2 = 33.7, C_3 = 1, C_4 = 135, C_5 = 33.75, C_6 = 70, C_7 = 550, C_8 = 1$ $C_9 = 200, C_{10} = 100, C_{11} = 80, C_{12} = 200, C_{13} = 30$
v_0	Potential when 50% of the firing rate is achieved	6 mV except for P_2 : 1mV
φ_0	Half of the maximum firing rate	2.5 Hz
r	Slope of the sigmoid function at v_0	0.56 mV^{-1}
φ_e	External input	φ_{e1} : pink noise with mean 200 Hz and standard deviation 30 Hz $\varphi_{e2} = 90 \text{ Hz}$

Appendix D. Model parameters and equations

The parameters of the model are described in Table D.1 and the equations are the following:

$$\begin{aligned}
 \hat{L}_1[u_1(t)] &= C_1 \sigma_{SS}(v_{SS}) \\
 \hat{L}_2[u_2(t)] &= C_2 \sigma_{SST}(v_{SST}) \\
 \hat{L}_3[u_3(t)] &= C_3 \varphi_{e1} \\
 \hat{L}_4[u_4(t)] &= C_4 \sigma_{P_1}(v_{P_1}) \\
 \hat{L}_5[u_5(t)] &= C_5 \sigma_{P_1}(v_{P_1}) \\
 \hat{L}_6[u_6(t)] &= C_6 \sigma_{P_2}(v_{P_2}) \\
 \hat{L}_7[u_7(t)] &= C_7 \sigma_{PV}(v_{PV}) \\
 \hat{L}_8[u_8(t)] &= C_8 \varphi_{e2} \\
 \hat{L}_9[u_9(t)] &= C_9 \sigma_{P_2}(v_{P_2}) \\
 \hat{L}_{10}[u_{10}(t)] &= C_{10} \sigma_{PV}(v_{PV}) \\
 \hat{L}_{11}[u_{11}(t)] &= C_{11} \sigma_{P_2}(v_{P_2}) \\
 \hat{L}_{12}[u_{12}(t)] &= C_{12} \sigma_{P_1}(v_{P_1}) \\
 \hat{L}_{13}[u_{13}(t)] &= C_{13} \sigma_{P_1}(v_{P_1})
 \end{aligned}$$

(D.1)

with neuronal population membrane potentials given by:

$$\begin{aligned}
 v_{P_1} &= u_1 + u_2 + u_3 + u_{11} \\
 v_{SS} &= u_4 \\
 v_{SST} &= u_5 \\
 v_{P_2} &= u_6 + u_7 + u_8 + u_{12} \\
 v_{PV} &= u_9 + u_{10} + u_{13}
 \end{aligned}
 \tag{D.2}$$

Appendix E. LaNMM contact couplings

Here we show the power correlation and the modulation index (MI) for the model LFP data. The power correlation is computed by extracting the amplitude of the band-passed signals using the Hilbert transform and then computing the Spearman correlation of the envelopes. The MI is computed as the entropy of the phase-amplitude histogram, with phase measured in the slow band and amplitude in the gamma band.

We show in Fig. E.1 that there is a generic negative power correlation between contacts. The most negative peak happens between the deep slow band and the superficial fast band for the best fit model parameters (box 4), and for the average over the best 0.1% model parameters from superficial to superficial layers (box 1).

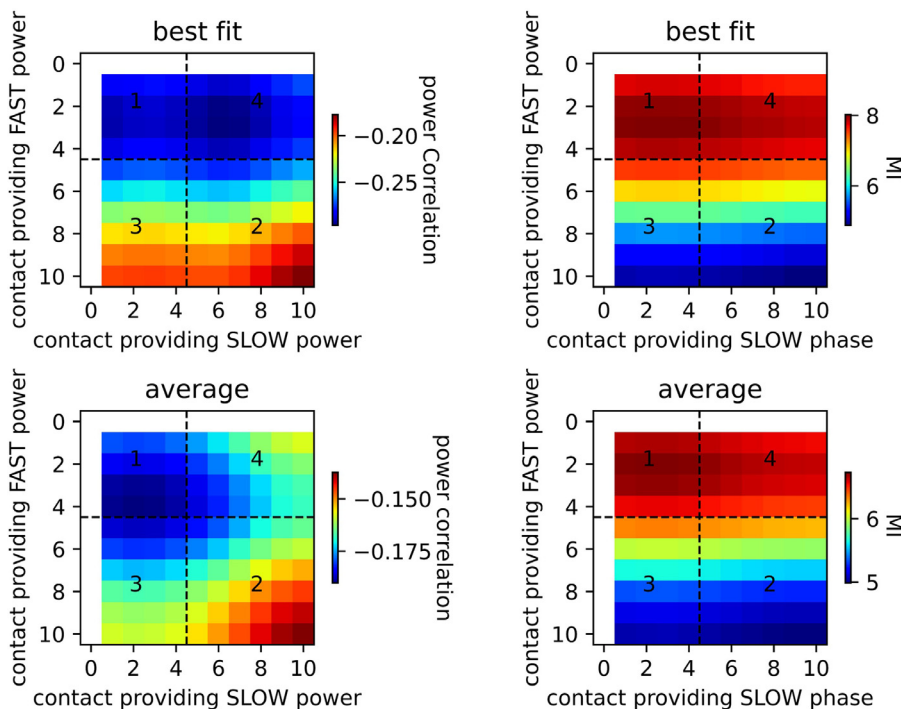


Fig. E.1. Power correlation (left) and modulation index (right) for the best model fit (top) and averaged over the best 0.1% model results. The dashed lines refer to the transitions between superficial and deep layers. The white rows indicate the reference contact.

In the case of MI, the model always displays a positive MI through all the contacts, with the peak in box 1, from superficial slow frequencies to superficial fast ones.

References

- Adams, R.A., Pinotsis, D., Tsirlis, K., Unruh, L., Mahajan, A., Horas, A.M., Convertino, L., Summerfelt, A., Sampath, H., Du, X.M., Kochunov, P., Ji, J.L., Repovs, G., Murray, J.D., Friston, K.J., Hong, L.E., Anticevic, A., 2022. Computational modeling of electroencephalography and functional magnetic resonance imaging paradigms indicates a consistent loss of pyramidal cell synaptic gain in schizophrenia. *Biol. Psychiatry* 91 (2), 202–215.
- Ahmadiadeh, S., Karoly, P.J., Ne, D., Grayden, D.B., Cook, M.J., Soudry, D., Free-stone, D.R., 2018. Bifurcation analysis of two coupled Jansen-Rit neural mass models. *PLoS ONE* 13 (3), 1–51. doi:10.1371/journal.pone.0192842.
- Bastos, A.M., Loonis, R., Kornblith, S., Lundqvist, M., Miller, E.K., 2018. Laminar recordings in frontal cortex suggest distinct layers for maintenance and control of working memory. *Proceedings of the National Academy of Sciences* 115 (5), 1117–1122. doi:10.1073/pnas.1710323115.
- Bastos, A.M., Urey, W.M., Adams, R.A., Mangun, G.R., Fries, P., Friston, K.J., 2012. Canonical microcircuits for predictive coding. *Neuron* 76 (4), 695–711. doi:10.1016/j.neuron.2012.10.038.
- Bastos, A.M., Vezoli, J., Bosman, C.A., Schoffelen, J.-M., Oostenveld, R., Dowdall, J.R., De Weerd, P., Kennedy, H., Fries, P., 2015. Visual areas exert feedforward and feedback influences through distinct frequency channels. *Neuron* 85 (2), 390–401. doi:10.1016/j.neuron.2014.12.018.
- Benwell, C.S.Y., Davila-Prez, P., Fried, P.J., Jones, R.N., Travison, T.G., Santarnecchi, E., Pascual-Leone, A., Shafi, M.M., 2020. EEG spectral power abnormalities and their relationship with cognitive dysfunction in patients with alzheimer's disease and type 2 diabetes. *Neurobiol. Aging* 85, 83–95. doi:10.1016/j.neurobiolaging.2019.10.004.
- Blomquist, P., Devor, A., Indahl, U.G., Ulbert, I., Einevoll, G.T., Dale, A.M., 2009. Estimation of thalamocortical and intracortical network models from joint thalamic single-electrode and cortical laminar-electrode recordings in the rat barrel system. *PLoS Comput. Biol.* 5 (3), e1000328. doi:10.1371/journal.pcbi.1000328.
- Bollimunta, A., Chen, Y., Schroeder, C.E., Ding, M., 2008. Neuronal mechanisms of cortical alpha oscillations in awake-behaving macaques. *The Journal of Neuroscience: The Official Journal of the Society for Neuroscience* 28 (40), 9976–9988. doi:10.1523/JNEUROSCI.2699-08.2008.
- Bollimunta, A., Mo, J., Schroeder, C.E., Ding, M., 2011. Neuronal mechanisms and attentional modulation of corticothalamic alpha oscillations. *The Journal of Neuroscience: The Official Journal of the Society for Neuroscience* 31 (13), 4935–4943. doi:10.1523/JNEUROSCI.5580-10.2011.
- Bonaio, J., Meyer, S., Little, S., Rossiter, H., Callaghan, M., Dick, F., Barnes, G., Bestmann, S., 2018. Laminar-specific cortical dynamics in human visual and sensorimotor cortices. *eLife* 7 (e33977).
- Borgers, C., Epstein, S., Kopell, N.J., 2008. Gamma oscillations mediate stimulus competition and attentional selection in a cortical network model. *Proceedings of the National Academy of Sciences* 105 (46), 18023–18028. doi:10.1073/pnas.0809511105.
- Buffalo, E.A., Fries, P., Landman, R., Buschman, T.J., Desimone, R., 2011. Laminar differences in gamma and alpha coherence in the ventral stream. *Proc. Natl. Acad. Sci. U.S.A.* 108 (27), 11262–11267. doi:10.1073/pnas.1011284108.
- Buzski, G., Anastasiou, C.A., Koch, C., 2012. The origin of extracellular fields and currents EEG, ECoG, LFP and spikes. *Nat. Rev. Neurosci.* 13, 407.
- Clusella, P., Köksal-Ersöz, E., Garcia-Ojalvo, J., Ruffini, G., 2022. Comparison between an exact and a heuristic neural mass model with second-order synapses. *Biol. Cybern.*
- Cole, S., Voytek, B., 2019. Cycle-by-cycle analysis of neural oscillations. *J. Neurophysiol.* 122 (2), 849–861. doi:10.1152/jn.00273.2019.
- David, O., Friston, K.J., 2003. A neural mass model for MEG/EEG: coupling and neuronal dynamics. *Neuroimage* 20 (3), 1743–1755.
- Deschle, N., Ignacio Gossn, J., Tewarie, P., Schelter, B., Daffertshofer, A., 2020. On the validity of neural mass models. *Front. Comput. Neurosci.* 14, 581040.
- Faugeras, O., Touboul, J., Cessac, B., 2009. A constructive mean-field analysis of multi-population neural networks with random synaptic weights and stochastic inputs. *Front. Comput. Neurosci.* 3, 1.
- Gieselmann, M.A., Thiele, A., 2022. Stimulus dependence of directed information exchange between cortical layers in macaque V1. *eLife* 11, e62949. doi:10.7554/eLife.62949. Publisher: eLife Sciences Publications, Ltd
- Godlove, D.C., Maier, A., Woodman, G.F., Schall, J.D., 2014. Microcircuitry of agranular frontal cortex: testing the generality of the canonical cortical microcircuit. *The Journal of Neuroscience: The Official Journal of the Society for Neuroscience* 34 (15), 5355–5369. doi:10.1523/JNEUROSCI.5127-13.2014.
- Goodfellow, M., 2011. Spatio-temporal Modelling and analysis of epileptiform EEG. The University of Manchester.
- Grimbert, F., Faugeras, O., 2006. Analysis of Jansen's model of a single cortical column. *INRIA RR-5597*, 34.
- Haegens, S., Barczak, A., Musacchia, G., Lipton, M.L., Mehta, A.D., Lakatos, P., Schroeder, C.E., 2015. Laminar profile and physiology of the alpha rhythm in primary visual, auditory, and somatosensory regions of neocortex. *The Journal of Neuroscience: The Official Journal of the Society for Neuroscience* 35 (42), 14341–14352. doi:10.1523/JNEUROSCI.0600-15.2015.
- Hagen, E., Nss, S., Ness, T.V., Einevoll, G.T., 2018. Multimodal modeling of neural network activity: computing LFP, ECoG, EEG, and MEG signals with LFPy 2.0. *Front Neuroinform* 12. doi:10.3389/fninf.2018.00092.
- Jansen, B.H., Rit, V.G., 1995. Electroencephalogram and visual evoked potential generation in a mathematical model of coupled cortical columns. *Biol Cybern* 73 (4), 357–366.
- Jansen, B.H., Zouridakis, G., Brandt, M.E., 1993. A neurophysiologically-based mathematical model of flash visual evoked potentials. *Biol Cybern* 68 (3), 275–283.
- Jaramillo, J., Mejias, J.F., Wang, X.-J., 2019. Engagement of pulvino-cortical feedforward and feedback pathways in cognitive computations. *Neuron* 101 (2), 321–336.e9. doi:10.1016/j.neuron.2018.11.023.
- Johnston, K., Ma, L., Schaeffer, L., Everling, S., 2019. Alpha oscillations modulate preparatory activity in marmoset area 8Ad. *J. Neurosci.* 39 (10), 1855–1866. doi:10.1523/JNEUROSCI.2703-18.2019.
- van Kerkoerle, T., Self, M.W., Dagnino, B., Gariel-Mathis, M.-A., Poort, J., van der Togt, C., Roelfsema, P.R., 2014. Alpha and gamma oscillations characterize feedback and feedforward processing in monkey visual cortex. *Proceedings of the National Academy of Sciences* 111 (40), 14332. doi:10.1073/pnas.1402773111.
- Kunze, T., Hunold, A., Hauelsen, J., Jirsa, V., Spiegler, A., 2016. Transcranial direct current stimulation changes resting state functional connectivity: a large-scale brain network modeling study. *Neuroimage* 140, 174–187. doi:10.1016/j.neuroimage.2016.02.015.
- Lee, S., Jones, S.R., 2013. Distinguishing mechanisms of gamma frequency oscillations in human current source signals using a computational model of a laminar neocortical network. *Front Hum Neurosci* 7. doi:10.3389/fnhum.2013.00869.
- Lefebvre, V., Zheng, Y., Martin, C., Devonshire, I.M., Harris, S., Mayhew, J.E., 2009. A dynamic causal model of the coupling between pulse stimulation and neural activity. *Neural Comput* 21 (10), 2846–2868. doi:10.1162/neco.2009.07-08-820.
- Leski, S., Pettersen, K., Tunstall, B., Einevoll, G., Gigg, D., DKWjck, J., 2011. Inverse current source density method in two dimensions: inferring neural activation from multielectrode recordings. *Neuroinformatics* 9 (4), 401–425.
- Lopez-Sola, E., Sanchez-Todo, R., Lleal, A., Kksal-Ersz, E., Yochum, M., Makhalova, J., Mercadal, B., Guasch-Morgades, M., Salvador, R., Lozano-Soldevilla, D., Modolo, J., Bartolomei, F., Wendling, F., Benquet, P., Ruffini, G., 2022. A personalizable autonomous neural mass model of epileptic seizures. *J Neural Eng* 19 (5), 055002. doi:10.1088/1741-2552/ac8ba8.
- Maier, A., Adams, G.K., Aura, C., Leopold, D.A., 2010. Distinct superficial and deep laminar domains of activity in the visual cortex during rest and stimulation. *Front Syst Neurosci* 4. doi:10.3389/fnsys.2010.00031.
- Maier, N., Nimrich, V., Draguhn, A., 2003. Cellular and network mechanisms underlying spontaneous sharp wave/ripple complexes in mouse hippocampal slices. *J. Physiol. (Lond.)* 550 (3), 873–887. doi:10.1113/jphysiol.2003.044602.
- Markov, N.T., Ercey-Ravasz, M., Van Essen, D.C., Knoblauch, K., Toroczkai, Z., Kennedy, H., 2013. Cortical high-density counterstream architectures. *Science* 342 (6158), 1238406. doi:10.1126/science.1238406. Publisher: American Association for the Advancement of Science
- Mejias, J.F., Murray, J.D., Kennedy, H., Wang, X.-J., 2016. Feedforward and feedback frequency-dependent interactions in a large-scale laminar network of the primate cortex. *Sci Adv* 14.
- Mercadal, B., Lopez-Sola, E., Galan-Gadea, A., Al Harrach, M., Sanchez-Todo, R., Salvador, R., Bartolomei, F., Wendling, F., Ruffini, G., 2022. Towards a mesoscale physical modeling framework for stereo-electro-EEG recordings. <https://www.biorxiv.org/content/10.1101/2022.07.06.498826v2>.
- Merlet, I., Biro, G., Salvador, R., Molae-Ardekani, B., Mekonnen, A., Soria-Frishi, A., Ruffini, G., Miranda, P.C., Wendling, F., 2013. From oscillatory transcranial current stimulation to scalp EEG changes: a biophysical and physiological modeling study. *PLoS ONE* 8 (2), 1–12. doi:10.1371/journal.pone.0057330.
- Miller, E.K., Lundqvist, M., Bastos, A.M., 2018. Working memory 2.0. *Neuron* 100 (2), 463–475. doi:10.1016/j.neuron.2018.09.023.
- Miranda, P.C., Mekonnen, A., Salvador, R., Ruffini, G., 2013. The electric field in the cortex during transcranial current stimulation. *Neuroimage* 70, 45–58.
- Mitzdorf, U., 1985. Current source-density method and application in cat cerebral cortex: investigation of evoked potentials and EEG phenomena. *Physiol Rev* 65 (37–100).
- Molae-Ardekani, B., Benquet, P., Bartolomei, F., Wendling, F., 2010. Computational modeling of high-frequency oscillations at the onset of neocortical partial seizures: from 'altered structure' to 'dysfunction'. *Neuroimage* 52 (3), 1109–1122.
- Montbrío, E., Pazó, D., Roxin, A., 2015. Macroscopic description for networks of spiking neurons. *Phys. Rev. X* 5 (2).
- Moran, R.J., Stephan, K.E., Kiebel, S.J., Rombach, N., O'Connor, W.T., Murphy, K.J., Reilly, R.B., Friston, K.J., 2008. Bayesian estimation of synaptic physiology from the spectral responses of neural masses. *Neuroimage* 42 (1), 272–284. doi:10.1016/j.neuroimage.2008.01.025.
- Muldoon, S.F., Pasquale, F., Gu, S., Cieslak, M., Grafton, S.T., Vettel, J.M., Bassett, D.S., 2016. Stimulation-based control of dynamic brain networks. *PLoS Comput. Biol.* 12 (9). doi:10.1371/journal.pcbi.1005076.
- Ninomiya, T., Dougherty, K., Godlove, D.C., Schall, J.D., Maier, A., 2015. Microcircuitry of agranular frontal cortex: contrasting laminar connectivity between occipital and frontal areas. *J. Neurophysiol.* 113 (9), 3242–3255. doi:10.1152/jn.00624.2014.
- Nunez, P.L., Srinivasan, R., 2006. Electric Fields of the Brain: The Neurophysics of EEG. Oxford University Press, USA.
- Palop, J.J., Mucke, L., 2016. Network abnormalities and interneuron dysfunction in Alzheimer disease. *Nat. Rev. Neurosci.* 17 (12), 777–792. doi:10.1038/nrn.2016.141.
- Pinotsis, D.A., Geerts, J.P., Pinto, L., FitzGerald, T.H.B., Litvak, V., Auksztulewicz, R., Friston, K.J., 2017. Linking canonical microcircuits and neuronal activity: dynamic causal modelling of laminar recordings. *Neuroimage* 146, 355–366. doi:10.1016/j.neuroimage.2016.11.041.
- Quairiaux, C., Megevand, P., Kiss, J., Michel, C., 2011. Functional development of large-scale sensorimotor cortical networks in the brain. *The Journal of Neuroscience* 31 (26), 9574–9584.

- van Rotterdam, A., Lopes da Silva, F.H., van den Ende, J., Viergever, M.A., Hermans, A.J., 1982. A model of the spatial-temporal characteristics of the alpha rhythm. *Bull. Math. Biol.* 44 (2), 283–305. doi:[10.1007/BF02463252](https://doi.org/10.1007/BF02463252).
- Sherman, S.M., Guillery, R.W., 1998. On the actions that one nerve cell can have on another: distinguishing drivers from modulators. *Proceedings of the National Academy of Sciences* 95 (12), 7121–7126. doi:[10.1073/pnas.95.12.7121](https://doi.org/10.1073/pnas.95.12.7121). Publisher: Proceedings of the National Academy of Sciences
- Lopes da Silva, F., A, v.R., Barts, P., Heusden, E., van Burr, W., 1976. Model of neuronal populations: the basic mechanism of rhythmicity. *Prog Brain Res* 45.
- Lopes da Silva, F.H., Hoek, A., Smits, H., Zetterberg, L.H., 1974. Model of brain rhythmic activity: the alpha rhythm of the thalamus. *Kybernetik* 15 (1), 27–37.
- Smith, M.A., Jia, X., Zandvakili, A., Kohn, A., 2013. Laminar dependence of neuronal correlations in visual cortex. *J. Neurophysiol.* 109 (4), 940–947. doi:[10.1152/jn.00846.2012](https://doi.org/10.1152/jn.00846.2012).
- Sotero, R.C., 2016. Topology, cross-frequency, and same-frequency band interactions shape the generation of phase-amplitude coupling in a neural mass model of a cortical column. *PLoS Comput. Biol.* 12 (11), e1005180. doi:[10.1371/journal.pcbi.1005180](https://doi.org/10.1371/journal.pcbi.1005180).
- Sotero, R.C., Bortel, A., Martinez-Cancino, R., Neupane, S., O'connor, P., Carbonell, F., Shmuel, A., 2010. Anatomically-constrained effective connectivity among layers in a cortical column modeled and estimated from local field potentials. *J. Integr. Neurosci.* 9 (04), 355–379. doi:[10.1142/S0219635210002548](https://doi.org/10.1142/S0219635210002548).
- Spaak, E., Bonnefond, M., Maier, A., Leopold, D.A., Jensen, O., 2012. Layer-specific entrainment of gamma-band neural activity by the alpha rhythm in monkey visual cortex. *Current biology: CB* 22 (24), 2313–2318. doi:[10.1016/j.cub.2012.10.020](https://doi.org/10.1016/j.cub.2012.10.020).
- Virtanen, P., Gommers, R., Oliphant, T.E., Haberland, M., Reddy, T., Cournapeau, D., Burovski, E., Peterson, P., Weckesser, W., Bright, J., van der Walt, S.J., Brett, M., Wilson, J., Millman, K.J., Mayorov, N., Nelson, A.R.J., Jones, E., Kern, R., Larson, E., Carey, C.J., Polat, A., Feng, Y., Moore, E.W., VanderPlas, J., Laxalde, D., Perktold, J., Cimrman, R., Henriksen, I., Quintero, E.A., Harris, C.R., Archibald, A.M., Ribeiro, A.H., Pedregosa, F., van Mulbregt, P., SciPy 1.0 Contributors, Vijaykumar, A., Bardelli, A.P., Rothberg, A., Hilboll, A., Kloeckner, A., Scopatz, A., Lee, A., Rokem, A., Woods, C.N., Fulton, C., Masson, C., Hggstrm, C., Fitzgerald, C., Nicholson, D.A., Hagen, D.R., Pasechnik, D.V., Olivetti, E., Martin, E., Wieser, E., Silva, F., Lenders, F., Wilhelm, F., Young, G., Price, G.A., Ingold, G.-L., Allen, G.E., Lee, G.R., Audren, H., Probst, I., Dietrich, J.P., Silterra, J., Webber, J.T., Slavi, J., Nothman, J., Buchner, J., Kulick, J., Schnberger, J.L., de Miranda Cardoso, J.V., Reimer, J., Harrington, J., Roldruez, J.L.C., Nunez-Iglesias, J., Kuczynski, J., Tritz, K., Thoma, M., Newville, M., Kmmmerer, M., Bolingbroke, M., Tartre, M., Pak, M., Smith, N.J., Nowaczyk, N., Shebanov, N., Pavlyk, O., Brodtkorb, P.A., Lee, P., McGibbon, R.T., Feldbauer, R., Lewis, S., Tygier, S., Sievert, S., Vigna, S., Peterson, S., More, S., Pudlik, T., Oshima, T., Pingel, T.J., Robitaille, T.P., Spura, T., Jones, T.R., Cera, T., Leslie, T., Zito, T., Krauss, T., Upadhyay, U., Halchenko, Y.O., Vaquez-Baeza, Y., 2020. Scipy 1.0: fundamental algorithms for scientific computing in python. *Nat. Methods* 17 (3), 261–272. doi:[10.1038/s41592-019-0686-2](https://doi.org/10.1038/s41592-019-0686-2).
- Xing, D., Yeh, C.-I., Burns, S., Shapley, R.M., 2012. Laminar analysis of visually evoked activity in the primary visual cortex. *Proceedings of the National Academy of Sciences* 109 (34), 13871–13876. doi:[10.1073/pnas.1201478109](https://doi.org/10.1073/pnas.1201478109).